Article

Current Biology

A change in behavioral state switches the pattern of motor output that underlies rhythmic head and orofacial movements

Graphical abstract

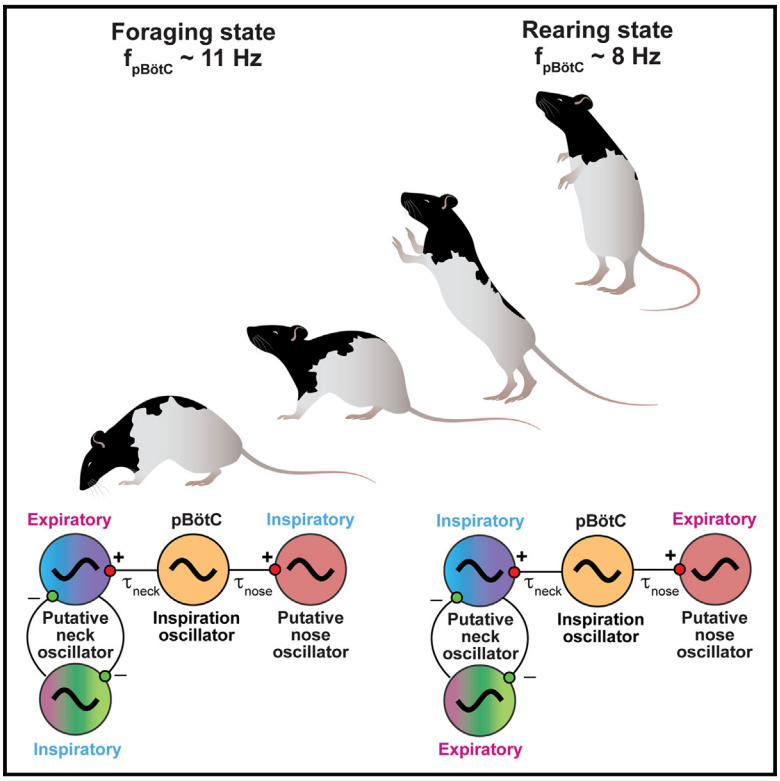

Highlights

- The rate of breathing as an animal searches will switch with behavioral state
- Rhythmic modulation of the yaw and pitch of head movement phase-locks to breathing
- The relative phase between head movement and breathing depends on behavioral state
- Coupled oscillators, without plasticity, can account for the state-dependent phases

Authors

Song-Mao Liao, David Kleinfeld

Correspondence

dk@physics.ucsd.edu

In brief

Liao and Kleinfeld report that orienting and orofacial movements lock to breathing in a state-dependent manner. Rodents transition between foraging and rearing states as they search. Each state is associated with a unique breathing rate and different phases of muscle activation relative to inhalation. This links sensory timing to behavioral state.

Liao & Kleinfeld, 2023, Current Biology *33*, 1–16
May 22, 2023
https://doi.org/10.1016/j.cub.2023.04.008

CellPress

Current Biology

CellPress

Article

A change in behavioral state switches the pattern of motor output that underlies rhythmic head and orofacial movements

Song-Mao Liao[1] and David Kleinfeld[1,2,3,*]
[1]Department of Physics, University of California San Diego, La Jolla, CA 92093, USA
[2]Department of Neurobiology, University of California San Diego, La Jolla, CA 92093, USA
[3]Lead contact
*Correspondence: dk@physics.ucsd.edu
https://doi.org/10.1016/j.cub.2023.04.008

SUMMARY

The breathing rhythm serves as a reference that paces orofacial motor actions and orchestrates active sensing. Past work has reported that pacing occurs solely at a fixed phase relative to sniffing. We re-evaluated this constraint as a function of exploratory behavior. Allocentric and egocentric rotations of the head and the electromyogenic activity of the motoneurons for head and orofacial movements were recorded in free-ranging rats as they searched for food. We found that a change in state from foraging to rearing is accompanied by a large phase shift in muscular activation relative to sniffing, and a concurrent change in the frequency of sniffing, so that pacing now occurs at one of the two phases. Further, head turning is biased such that an animal gathers a novel sample of its environment upon inhalation. In total, the coordination of active sensing has a previously unrealized computational complexity. This can emerge from hindbrain circuits with fixed architecture and credible synaptic time delays.

INTRODUCTION

Many natural behaviors in animals involve significant rhythmic components. First and foremost, these encompass locomotion and orienting, the essential motor actions for navigation, through the coordination of brainstem and spinal motor plants.[1–3] The kinematics of locomotion are well studied,[4] and the dynamics are computationally rich. In particular, the relative timing among the muscle groups that drive the limbs in tetrapeds will change as the speed of the animal increases and the gait progresses from walking to jogging to trotting to cantering and lastly to galloping.[5,6] This can be solely enabled by phase shifts that accumulate in networks of oscillators with time-delayed connections.[7–11] A similar dynamic occurs in networks that govern undulatory locomotion.[12] In contrast to the case of locomotion, relatively little is known about the kinematics and dynamics of orienting motor actions. One claim that motivates this work is that vertical head bobbing, i.e., changes in pitch, is phase-locked to breathing as rodents explore their environment.[13–15]

Beyond head bobbing, the breathing rhythm plays an outsized role in the coordination of orofacial motor actions in rodents.[13,16] Quantitative measurements of the coordination of orofacial motor control by breathing were reported for whisking,[17–22] facial movement via the mystacial pad,[17] and nose twitching[14] with freely moving rodents that inhabited a small platform. In all cases, the movement was locked to a single phase in the breathing cycle. These results led to the "master oscillator" hypothesis, where breathing serves as the reference oscillator to bind orofacial sensory inputs.[16,23,24] In principle, this permits sensory information from multiple modalities to be gathered with a precise temporal relationship for efficient and accurate neuronal computations. In fact, recent evidence[15,25] supports the role of the respiration cycle as a reference oscillator in high-level sensory and cognitive processing.[26,27] Yet, all known past studies on the phase of motor actions with respect to breathing, and on the phase of computational actions with respect to breathing, report that locking occurs solely at a single, fixed phase.[13,14,17,28,29] This implies a surprisingly harsh constraint on the combinatorics that govern the coordination of different actions into behaviors.

We believe that the sparsity of ethological context in the foundational studies[13–22,25–27] had the untold effect of limiting our discovery of a potentially richer computational complexity. We thus hypothesize that the coordination of motor actions with breathing can exhibit multiple, stable phase relations when rodents can switch among different ethological contexts. We test this hypothesis using a behavioral task that involves exploration, navigation, and active sensation as rats search for and ingest food in a large arena. We ask that (1) does the frequency of sniffing change with behavioral state? This question is motivated by a change in sniffing frequency between odor sampling and reward selection in a forced-choice task.[30] (2) Does the coordinated constriction among neck and orofacial muscles relative to themselves, as well as to breathing, depend on behavioral state? This question is motivated by changes in gait concurrent with changes in the speed of locomotion.[31,32] (3) How does activation of the musculature involved in head turning and nose turning coordinate with breathing, as well as respect the midline as an axis of symmetry? This addresses the question of when rodents

Please cite this article in press as: Liao and Kleinfeld, A change in behavioral state switches the pattern of motor output that underlies rhythmic head and orofacial movements, Current Biology (2023), https://doi.org/10.1016/j.cub.2023.04.008

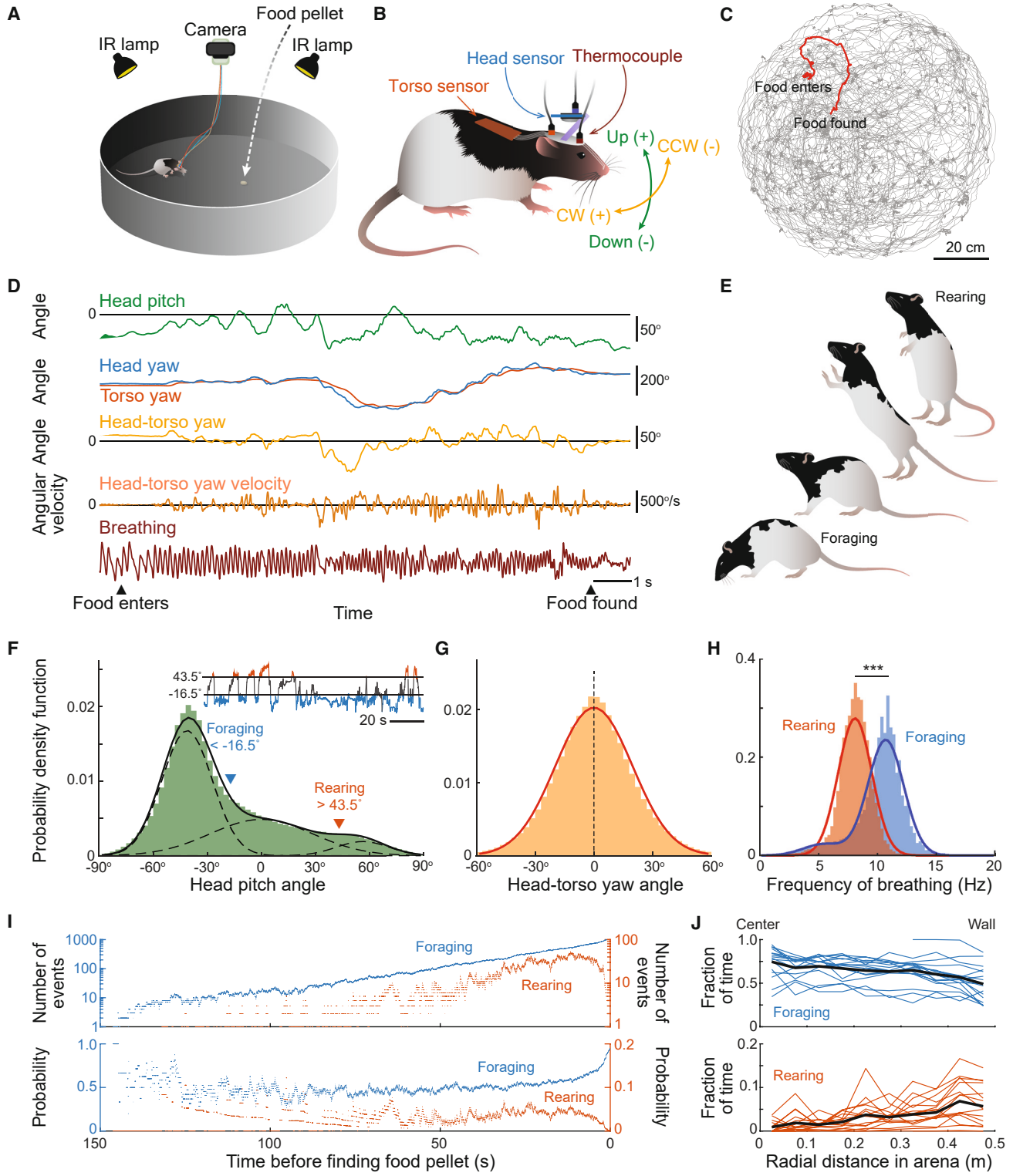

Figure 1. Head movements and breathing in foraging and rearing rats

(A) Depiction of the foraging task in the circular arena, 1 m in diameter.

(B) Depiction of movements of the head and torso that are measured with orientation sensors and breathing with a thermocouple from freely moving rats. We define the horizontal (yaw) angular velocity to be positive when the rotation is clockwise (CW) and negative when the rotation is counterclockwise (CCW), as viewed from above. The vertical (pitch) angle is defined as positive when the head is raised up against the gravity and is defined as negative when the head is tilted downward.

(legend continued on next page)

Please cite this article in press as: Liao and Kleinfeld, A change in behavioral state switches the pattern of motor output that underlies rhythmic head and orofacial movements, Current Biology (2023), https://doi.org/10.1016/j.cub.2023.04.008

should best sample their environment as they rotate their head and nose outward with respect to their midline. Motivated by prior work on horizontal head movement in mice,[33] we monitored head orientation and head turns relative to the torso, along with the activation of muscles that drive head motion and the orofacial actions of the nose and face.

RESULTS

We trained 33 food-restricted rats to search in the dark for food within an open circular arena of 1 m in diameter (Figure 1A). A nine-axis absolute orientation sensor was mounted onto the skull to measure acceleration of the head in Euclidian coordinates, the three-dimensional angular velocity in Euler coordinates, and the absolute orientation, i.e., yaw, pitch, and roll, at 100 Hz (Figure 1B); these define movement in allocentric coordinates. In 17 animals, a second absolute orientation sensor was embedded subcutaneously to measure movement and orientation of the torso (Figure 1B). The torso sensor signals were subtracted from the head sensor signals to obtain the relative head-torso orientation and angular velocities; these define movement in egocentric coordinates.[34] The difference in sensor orientation was found to drift by less than 0.01° over the period of recording. In all animals, respiration was recorded by an implanted thermocouple in the nasal cavity that measured the cyclic change in air temperature concurrent with inhalation and expiration (Figure 1B). We used a Hilbert transform to locate the onsets of inspiration, which we took as the start of each breathing cycle with a phase of 0 radians. Videography was used to track the position of the animal in the arena (Figures 1B and 1C).

Behavioral states are revealed when animals search inside an arena

Small, regularly sized pellets of food were individually dropped at a random location in the arena after an auditory clue (Figure 1A). The rats were observed to travel along approximate curvilinear arcs that spanned the entire arena as they searched for a pellet and then lapped the pellet with their tongue and swallowed. After a brief delay, the process started anew. Each rat executed rich head movements in both the horizontal (yaw) and vertical (pitch) directions in the search for food. Figure 1D shows an example measurement of head-torso movement and breathing in a trial where the animal was locomoting and sniffing with its head downward to the floor in an act designated as foraging (Figure 1E). On occasion, the rat paused its locomotion and rose up on its hind legs to head-bob and sniff in an act designated as rearing (Figure 1E). We used the instantaneous head pitch angle to categorize these behavioral states across a population (29 rats) in terms of the probability density of the head pitch angle (Figure 1F). The distribution is well fit with three Gaussians ($r^2 = 0.983$; Figure 1F). The intersections between neighboring Gaussians provides a conservative metric to define a threshold pitch for the foraging state, i.e., head pitch below −16.5°, and a threshold for the rearing state, i.e., head pitch above 43.5° (Figures 1F and S1A). Lastly, while the distribution of head pitch angles is multimodal (Figure 1F), the distribution of the head-torso yaw angle, i.e., head turning in the horizontal plane, is well fit by a single Gaussian distribution that is centered at zero ($r^2 = 0.992$; Figure 1G).

The distribution of sniffing frequencies associated with rhythmic head-torso turning was found to depend on the behavioral state of the rat (Figure 1H). Foraging occurred with a frequency centered near 11 Hz, while rearing occurred at a lower frequency centered near 8 Hz. The separation of center frequencies for the two states was significant ($p < 0.001$ across 32 of 33 rats). All told, foraging is defined by a low pitch angle and a higher breathing rate, while rearing is defined by a high pitch angle and a lower breathing rate (Figures 1E, 1F, and 1H). While foraging and rearing were interspersed across time (inset in Figure 1F), the foraging mode dominated the behavior as the rat approached the food pellet (Figure 1I). Rearing events were more frequent as the rat searched closer to the arena wall since rats must rear to search along a wall (Figure 1J).

Head movements phase-locked to breathing during both foraging and rearing

Past work established that changes in the pitch of an animal's head while it explored is locked to the breathing rhythm.[14] Here, we further observed that head-torso turning in the horizontal plane, i.e., egocentric movement, is rhythmic with two spectral components. The movement involves the waxing and waning of a slow spectral component below 5 Hz, the frequency band for orienting and basal breathing, as well as a fast component centered near 10 Hz (Figure 2A), the frequency of sniffing (Figure 1H). These spectral components also appear in absolute

(C) Trajectories of 72 foraging trials for one rat as traced by DeepLabCut. The path in (D) is highlighted in red.
(D) Example data of the pitch angle of the head, the yaw angle of the head, torso, and head-torso, the yaw velocity of head-torso, and breathing in one foraging rat. Left arrowhead indicates the time when the food pellet is dropped into the arena and the right arrowhead the time when the rat finds the food. The spectrogram of these data appears in Figure 2A. We chose the polarity of the thermocouple signal so that increasing values, i.e., rising and positive slope, indicate inhaling and decreasing values, i.e., negative slope, indicate exhaling.
(E) Illustration of rodent behaviors that are formed with foraging and rearing states.
(F) Probability density distribution of the head pitch angle. Data pooled from 29 rats. Distribution is fitted by three Gaussians. Intersections of the Gaussian fits at −16.5° and 43.5° are labeled and used as the thresholds to define the behavioral states. Insert: example time series of the pitch angle; see also Figure S1A.
(G) Probability density distribution of the head-torso yaw angle. Data pooled from 17 rats. Red line indicates the Gaussian fit (mean = 0, SD = 19.7°).
(H) Probability density distribution of the periods of breathing cycles in foraging and rearing states. Data pooled from 33 rats. Rearing and foraging distributions are fitted with one and two Gaussians, respectively. Mean, standard deviation, and relative amplitude of the fit (mean, SD, relative amplitude) are (8.1 Hz, 1.4 Hz, 1.0) for rearing; (5.5 Hz, 1.8 Hz, 0.10) and (10.7 Hz, 1.5 Hz, 0.90) for foraging. p value calculated using Kolmogorov–Smirnov test.
(I) Number of foraging and rearing events (top) and corresponding probabilities (bottom) with respect to the time for the rat to find and consume food. Data pooled from 1,167 foraging trials collected from 10 rats.
(J) Fractions of time spent foraging (top) versus rearing (bottom) as a function of radial distance inside the arena. Data pooled from 17 rats. Averages were shown in black; the slopes of a linear regression are significant for both cases, with $p < 0.001$. Note that the sum of probabilities is less than one as some events are neither foraging nor rearing.

Please cite this article in press as: Liao and Kleinfeld, A change in behavioral state switches the pattern of motor output that underlies rhythmic head and orofacial movements, Current Biology (2023), https://doi.org/10.1016/j.cub.2023.04.008

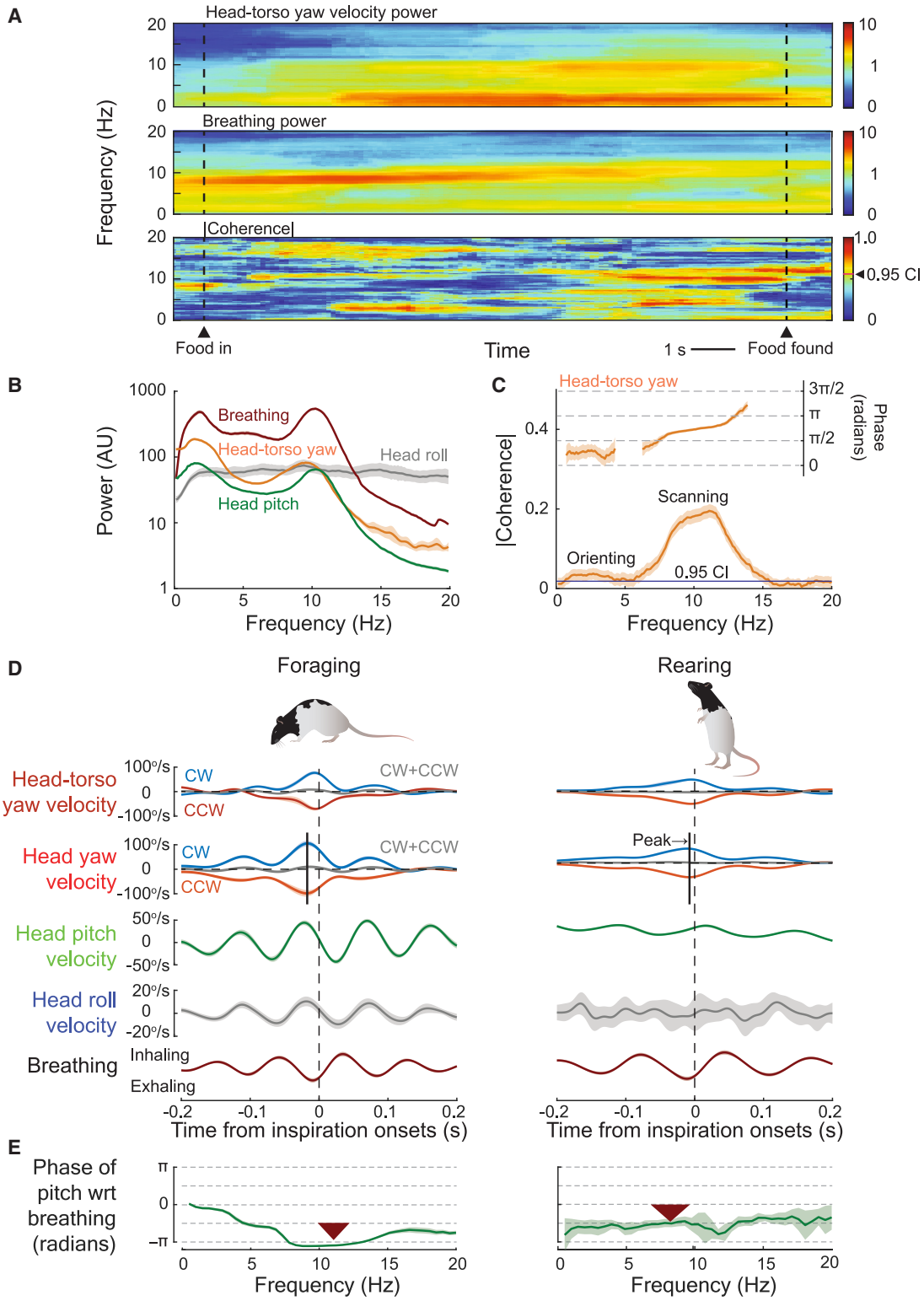

Figure 2. Head movement is phase-locked to breathing with a phase modulated by posture

(A) Spectrogram of the head-torso yaw velocity, i.e., power in the velocity versus time (top), spectrogram of breathing (middle), and their spectral coherence (bottom) from data shown in Figure 1D. Red band in the coherence indicate close tracking of yaw velocity and breathing. Spectra and coherence are calculated with a moving window of width 5 s and a 0.1 s step size. The half-bandwidth is 1 Hz (9 tapers), and the 0.95 confidence level is $|C| = 0.56$.

(legend continued on next page)

Please cite this article in press as: Liao and Kleinfeld, A change in behavioral state switches the pattern of motor output that underlies rhythmic head and orofacial movements, Current Biology (2023), https://doi.org/10.1016/j.cub.2023.04.008

rotations in head yaw, i.e., allocentric movement, along with head pitch and breathing (Figure 2B). To quantify the relation of egocentric yaw to breathing, we calculated the spectral coherence between head-torso yaw and breathing, a measure of how well these two rhythms track over time. Indeed, the two rhythms are strongly phase-locked in the 8–12 Hz band, albeit weakly phase-locked in the 1–5 Hz band, that encompasses rhythmic head turning. Here, and elsewhere in the manuscript, phase-locking is defined as a statistically significant magnitude of the coherence at the frequency in question (Figures 2A and 2C).

Is the timing between head movements and breathing the same during foraging versus rearing? We considered egocentric head-torso turns and all allosteric head turns, divided the time series of movements into epochs with clockwise (CW) versus counterCW (CCW) yaw movements and calculated the correlation between the angular velocity of each movement and breathing (Figure 2D). We observed that head-torso yaw-angular velocity is rhythmic and phase-locked to breathing for both foraging and rearing. The peak amplitude occurs close to that of the onset of inspiration for both CW and CCW movements, and the time lag is 11 ms greater for foraging than rearing (fiducial lines, Figure 2D). Lastly, phase-locking is also observed for allocentric head yaw-angular velocity and breathing (Figure 2D). As a control, the correlation between yaw movement and breathing was lost when the sum of the two directions is considered (black curve, Figure 2D), confirming that the rat makes approximately equal numbers of CW versus CCW movements in the foraging state; $(N_{CCW} - N_{CW})/(N_{CCW} + N_{CW}) = -0.004 \pm 0.018$ for egocentric head turning (N_{CCW} and N_{CW} calculated over all trials for each of 17 rats, with 254 trials total, and the ratio is averaged over all rats) and -0.017 ± 0.028 for allocentric head turning (471 total trials and an average across 33 rats).

The timing for the angular velocity of head pitch relative to breathing advances from roughly a quarter cycle after the onset of inspiration to roughly a quarter cycle before the onset. This is half a cycle in total or equivalently π radians in phase, as the rat changes state from foraging to rearing (Figure 2E). In contrast to the cases of yaw and pitch, the correlation of head roll angular velocity with breathing is apparent during foraging but is essentially absent during rearing (gray curve, Figure 2D). All told, these data show that changes in behavioral state lead not only to a shift in the frequency of breathing (Figure 1H), but also a shift in the phase relation between breathing and both egocentric and allocentric movement of the head (Figures 2C–2E).

Neck muscles phase-locked to breathing during both foraging and rearing

The movement of the head is controlled by a multiplicity of muscles.[35] To record the motor outputs directly from the musculature that contributes to the sniffing-correlated head movements, we measured the electromyogram (EMG) from three ventrolateral neck muscles, i.e., the sternomastoid (SM) (3 bilaterally and 4 unilaterally implanted rats), cleidomastoid (CM) (4 bilateral and 4 unilateral), and clavotrapezius (CT) (6 bilateral and 5 unilateral), and two dorsal neck muscles, i.e., the splenius (SP) (6 bilateral and 4 unilateral) and biventer cervicis (BC) (3 bilateral and 4 unilateral) (Figure 3A). Figures 3B–3D show three example sets of raw and processed EMG data, the latter to indicate the envelope of muscle excitation, along with egocentric head movement and breathing. In general, we obtained between 3 and 6 measurements for each of the five muscle groups across the two sides of the body (Table S1).

The activities of all five neck muscles were phase-locked with head movements (Figures S1B–S1D), thus confirming their individual roles as drivers of head movement. We further observed that the activation of all five neck muscles were correlated with the onset of sniffing (Figure 3E). The detailed pattern of activity was modulated by the rat's posture, i.e., its head pitch angle (Figure 3E). The sternomastoid muscle is unique in that it has the greatest amplitude of modulation for rearing, in concordance with the associated change in pitch. All other ventral and dorsal muscles have a greater amplitude and present a simpler rhythmic pattern during foraging as opposed to rearing.

Vibrissa, facial, and nose muscles lock to breathing for both foraging and rearing

We revisited the coordination of three orofacial motor actions with breathing, i.e., whisking,[14,17] retraction of the mystacial pad,[17] and nose twitching,[14,38] in light of our finding that different patterns of movement and muscular control are revealed by changes in posture (Figures 2 and 3). For whisking, we recorded the EMG from the intrinsic protractor (VI) muscles[39–41] (5 rats) (Figure 4A). For movement of the pad, we recorded the EMG from the extrinsic vibrissa muscle nasolabialis[39,42] (NL) (3 rats) (Figure 4A), which further retracts the vibrissae by pulling their exit point from the follicles toward the back.[39] To measure nose twitching, we recorded the EMG from the deflector nasi (DN) muscle[43] (7 rats) (Figure 4A). This muscle pulls the nose upward and lateral under ipsilateral activation and pulls solely upward under bilateral coactivation.[14] Figures 4B and 4C shows two sets of example EMG recordings, along with breathing and head movements as the rat foraged. In general, we obtained 3 or 4 measurements for each of these three muscle groups across the two sides of the body (Table S1).

Similar to the neck muscles (Figure 3E), we observed a shift in the timing of activation of the orofacial muscles with the onset of inspiration as a function of the pitch angle (Figure 4D). A change in the shape of the waveform from sine- to sawtooth-like is seen

(B) Spectra of breathing, head pitch velocity, head roll velocity, and head-torso yaw velocity, shown with jackknife error bars. Data from one rat; 582 windows of size = 4 s, half-bandwidth = 1 Hz (7 tapers). Note peaks at 2 and 11 Hz.

(C) Coherence of head-torso yaw velocity with breathing during foraging. Data, from the same rat as in (B), shown with jackknife error bars; 582 windows of 4 s in width, half-bandwidth of 2 Hz (15 tapers). Horizontal line indicates 0.95 confidence level.

(D) Summary of egocentric head yaw and allocentric head movements relative to the onset of inspiration. Error bars are standard errors across rats. Data of egocentric movements pooled from 17/15 rats in the foraging/rearing states. Data of allocentric movements pooled from 33/31 rats in the foraging/rearing states. Two rats did not have rearing epochs longer than 0.4 s for averaging.

(E) Phase of the statistically significant regions of the coherence between head pitch velocity and breathing using the data of (D); the half-bandwidth is 2 Hz. Note the shift in phase of about $\pi/2$ radians between foraging and rearing, which shows that phase is modulated by posture. The arrows point to the center frequency of sniffing, and the width is the FWHM of the associated distribution (Figure 1H).

Please cite this article in press as: Liao and Kleinfeld, A change in behavioral state switches the pattern of motor output that underlies rhythmic head and orofacial movements, Current Biology (2023), https://doi.org/10.1016/j.cub.2023.04.008

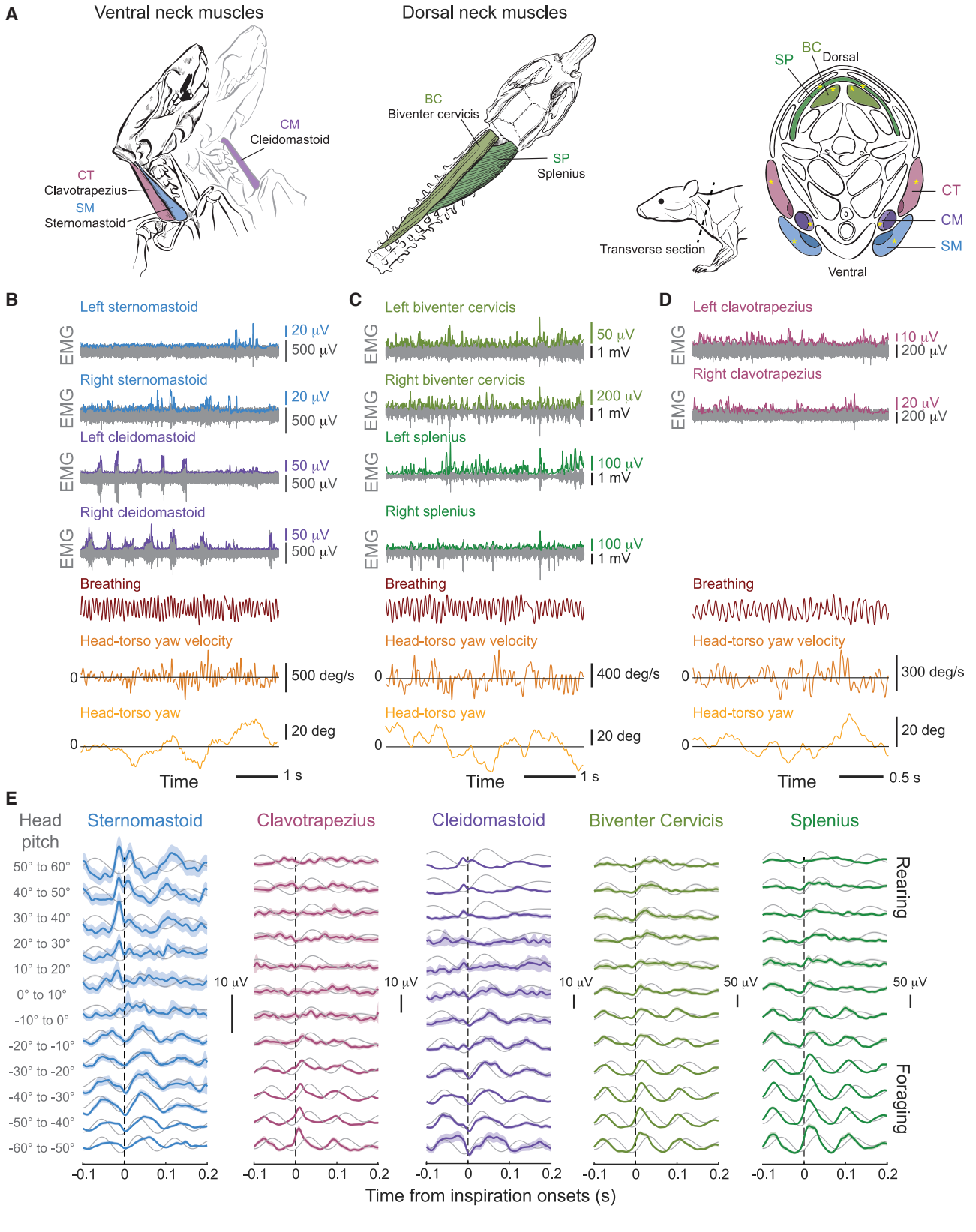

(legend on next page)

Please cite this article in press as: Liao and Kleinfeld, A change in behavioral state switches the pattern of motor output that underlies rhythmic head and orofacial movements, Current Biology (2023), https://doi.org/10.1016/j.cub.2023.04.008

for intrinsic muscle activity (3 rats) in the transition from foraging to rearing, i.e., increasing pitch angle, although timing is largely unchanged. In contrast to the case for the intrinsic muscle, NL activity (3 rats) and DN activity (7 rats) are retarded in time across the transition from foraging to rearing. All told, a change in behavioral state from foraging to rearing affects the timing of orofacial (Figure 4) as well as orienting (Figure 3) motor actions.

Shifts in phase among motor actions and breathing between foraging and rearing

To gain further insight into the temporal changes in muscular control between the states of foraging versus rearing, we divided the EMG data for the five neck muscles according to the state of animals: the foraging state, with head pitch angle less than -16.5°, and the rearing state, with angle greater than 43.5° (Figure 1F); responses at the intermediate angles between -16.5° and 43.5° were not further characterized. These datasets were found to cluster into two subgroups. The first subgroup consists of the SM and CM muscles. During foraging, these two muscles are maximally activated upon exhalation (Figure 5A). When the animal switched from the foraging to the rearing state, the activities of these muscles dramatically shifted to coincide with the onset of inspiration. The second subgroup consists of the CT, SP, and BC muscles. These three muscles were maximally activated just after the onset of inspiration as the rat foraged, with a phase difference of about -0.75π radians compared with the first subgroup (Figure 5A). Here, when the animal switched from foraging to rearing, the modulation of the CT, SP, and BC muscles by breathing is diminished and shifted toward a peak modulation at expiration. The phase difference between muscle subgroups is maintained. All told, these data show that the behavioral state will change the motor output of specific muscles that set the phase of rhythmic head movement with respect to breathing.

An alternate means to analyze the relation of muscle activity and breathing is in terms of spectral analysis. All five pairs of neck muscles were significantly modulated by breathing during both foraging, at 8–14 Hz, and rearing, at 6–11 Hz (Figure 5B); the range of frequencies for significance is consistent with the observed sniffing rate (Figures 1H and 5B). Four of the five neck muscles, i.e., the SM, CM, SP, and BC, shifted their phases with respect to breathing by $\sim\pi$ radians as the animal switched between foraging and rearing (Figure 5B). The exception is the CT muscle, which is in phase with the SP and BC muscles during foraging, but only it shifted its phase relationship with breathing by $\sim \pi/2$ radians when the animal switched to rearing. Thus, the phase relationship of the CT muscle with respect to sniffing lies between the inspiratory (INS), i.e., SM and CM, and expiratory (EXP), i.e., SP and BC, subgroups of muscles during rearing (Figure 5B).

We turn to a similar analysis for motor control of the vibrissae, mystacial pad, and nose. During foraging, the intrinsic vibrissa muscles (4 bilaterally and 1 unilaterally implanted rat) are activated at the start of inspiration, with the retractor NL (3 bilateral) activated after a delay (Figure 5C). Interestingly, the EMG envelope of the DN muscle (3 bilateral and 4 unilateral) consists of two peaks, one in the middle and one at the end of inspiration; this "double pump" was missed in the relatively sparse dataset of prior work.[14] The detailed pattern of activation shifted during rearing. A small change occurred for the intrinsic muscles, which are activated closer to the onset of inspiration, and for the retractor NL, which is activated later in the sniff cycle. A large change occurred for the DN muscle, which is now activated during expiration (Figure 5C). Surprisingly, the activation patterns of these underlying muscles resemble the findings previously reported for head-fixed animals.[19,38,39,44]

The peak activity of each muscle group as a function of phase in the sniff cycle was found from the spectral coherence (Figure 5D), similar to the case for neck muscles. The phase shifts for the intrinsic and NL muscles are small, about $\pi/4$ radians, between foraging and rearing. In contrast, the DN shifts its phase relationship with breathing by $\sim 0.65\pi$ radians when the animal switches to rearing (Figure 5D).

To further explore the dynamics of nose movements (3 rats), we formed a raster plot of the right DN muscle peaks with respect to the left peaks (Figure S2A), as well as their coherence (Figure S2B). Bilateral coactivation of DN muscle predominates under all conditions, yet unilateral activation is more prevalent during foraging than during rearing (Figures S2A and S2B). Thus, the rat performed more extensive lateral nose movements during foraging. Further to this point, nose twitching was phase-locked to head movement during both foraging and rearing (Figure S2C). Yet, activation of the DN muscle lags activation of the CT muscle during foraging but precedes activation of the CT muscle during rearing. The most salient observation is that the vibrissa intrinsic and the DN muscles on the side of the head ipsilateral to a head turn have greater magnitudes than those on the contralateral side (Figure S2D). This confirms that head turning is accompanied by asymmetric whisking, with the ipsilateral vibrissae more protracted.[45,46] From the perspective of

Figure 3. Electromyogenic recording from neck muscles during full arena search

(A) (Left) Anatomical depiction of ventral neck muscles sternomastoid (SM), cleidomastoid (CM), and clavotrapezius (CT). (Middle) Anatomical depiction of dorsal neck muscles splenius (SP) and biventer cervicis (BC). (Right) Transverse section (dashed line) showing the relative locations of the muscles. Yellow asterisks indicate the locations where the electromyogram (EMG) signals are recorded. Illustrations adapted from the work of Peterson.[36,37]

(B) Example EMGs from bilateral sternomastoid and cleidomastoid muscles (gray), along with the processed data to yield the envelope of muscle activation, and the concurrent breathing and head-torso yaw movements. Data from one rat.

(C) Example EMGs from bilateral biventer cervicis and splenius muscles (gray); otherwise as above.

(D) Example EMGs from bilateral clavotrapezius; otherwise as above.

(E) Cross-correlation of the EMG envelopes of all five neck muscles with respect to the onset of inspiration (sniffing, 4–14 Hz) and as a function of head pitch angle. Shaded areas indicate the standard errors. Data from individual rats. Number of inspiration onsets (foraging/uncategorized/rearing): SM (4,098/1,186/380); CM (2,671/862/1,030); CT (2,632/906/368); SP (4,836/1,122/473); and BC (5,199/808/144). Except for the sternomastoid muscle, correlations are stronger during foraging. The gray traces are the autocorrelations of sniffing.

See also Figure S1 and Table S1.

Please cite this article in press as: Liao and Kleinfeld, A change in behavioral state switches the pattern of motor output that underlies rhythmic head and orofacial movements, Current Biology (2023), https://doi.org/10.1016/j.cub.2023.04.008

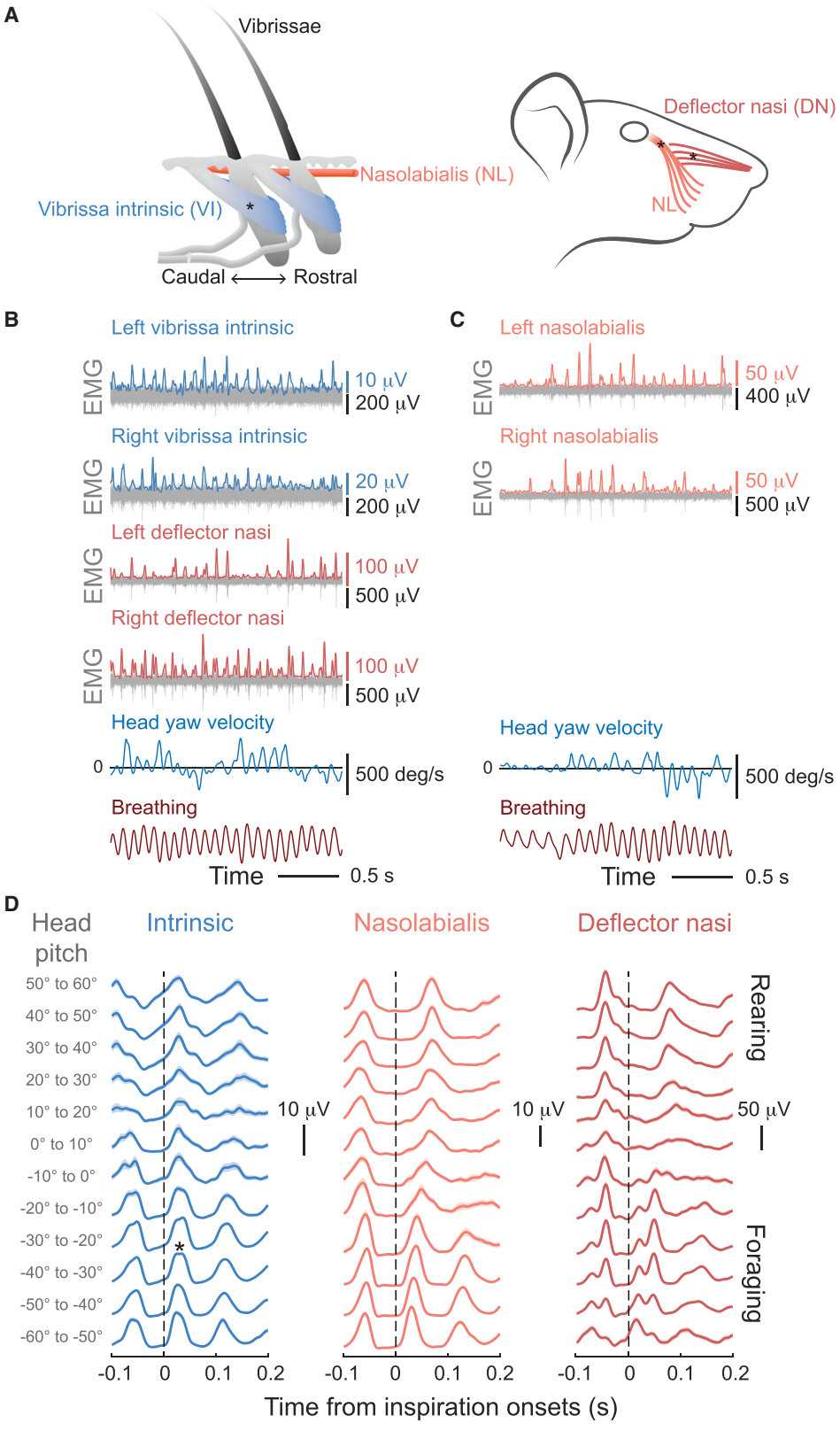

(legend on next page)

Please cite this article in press as: Liao and Kleinfeld, A change in behavioral state switches the pattern of motor output that underlies rhythmic head and orofacial movements, Current Biology (2023), https://doi.org/10.1016/j.cub.2023.04.008

behavior, these observations imply that the nose is drawn to the maximum lateral extent of a turn during foraging, consistent with efficient localization of an odor source.[38]

Inspiration occurs at the transition from outward to inward horizontal turns

We have shown that egocentric, head-torso movements are phase-locked with breathing (Figures 2A–2C). Yet, horizontal head movements must also respect the midline, i.e., the symmetry axis of the body. To study the potential relationship between the timing of head-torso yaw movements and breathing relative to the midline, we separately analyzed the cases of egocentric CCW and CW head rotations during foraging. We identified the peaks in the head-torso yaw velocity for both directions of rotations (Figure 6A) and plotted the locations of the peaks with respect to the onset of inspiration as a raster (Figure 6B). For both CCW and CW head turns, the location of the peaks forms two clusters within the spectral band of sniffing. One cluster occurs during the inspiratory (INS) phase of a head turn and the other during the expiratory (EXP) phase (Figure 6B). We denote the four clusters as INS-CCW and INS-CW head turns and as EXP-CCW and EXP-CW head turns (Figure 6C).

We found that the division of inspiration and expiration events depends on the location of the head relative to the midline of the animal ($p < 0.001$ in 16 of 17 rats, Kolmogorov-Smirnov test) (Figure 6D). Inward turns, i.e., toward the midline, are more likely to occur during inspiration for both CCW and CW head rotations (Figure 6E). As such, the initiation of outward turns, i.e., away from the midline, are more likely to occur during expiration (Figure 6E). Thus, the next INS event during an outward turn occurs with the head at maximum rotation. This ensures a fresh sampling of the environment.

We summarized the sequence of neck muscle recruitments during the sniffing cycles by combining the data for movement (Figures 6C and 6D) with the EMG recordings from neck muscles (Figures 5A and 5B). Upon the onset of inspiration, the CT, BC, and SP muscles are recruited to turn the head inward (Figure 6F). At the transition from inhalation to exhalation, the SM and CM muscles are recruited and turn the head outward (Figure 6F). The inward versus outward dependence of horizontal head movement with sniffing is less evident when the rat is in the rearing state ($p = 0.0013$ for CCW and $p = 0.16$ for CW head movements; Kolmogorov-Smirnov test) (Figure S3A and S3B).

Other features may contribute to the division of INS versus EXP head turns. We find a bimodal distribution for the radial location in the arena ($p < 0.01$ in 5 of 17 rats, Kolmogorov-Smirnov test) (Figures S3C and S3D), for the locomotion speed ($p < 0.001$ in 11 of 17 rats, Kolmogorov-Smirnov test) (Figure S3E), and for the instantaneous speed of the head turn ($p < 0.001$ in 16 of 17 rats, Kolmogorov-Smirnov test) (Figure S3F). In general, the maximal head-speed during EXP turns is greater than the maximal speed in INS turns (Figure S3F).

The activation of all five neck muscles relative to breathing has a peak at zero lag time (Figures S1D and S3G). This indicates that bilateral muscles are coactivated, as occurs at most joints,[47] and the net torque determines the resultant direction of the head rotation. Yet, the CM muscle, unlike the other four neck muscles, showed peaks at ± 0.25 s in the cross-correlation between its left and right instantiations (Figure S3G); this is in addition to its participation in synergistic control of head turning (Figures 3 and 5). Thus, the CM muscle is also responsible for controlling the slow component of the horizontal head orientation (Figure 2B), during which the EMG envelope of the ipsilateral CM muscle exhibits a sequence of peaks that correspond to small, successive head rotations across several sniffs (Figure S3H).

DISCUSSION

Our first claim involves the modulation of breathing, the fundamental rhythm of life, and the possibility that breathing may serve as a proxy for behavioral state. When rodents switch from foraging, with their vibrissae sweeping across the ground and their nose scanning the air just above, to the state of rearing, when they rise on their hind legs, their breathing rate decrements by 3 Hz (Figure 1H). This change in behavioral state is associated with a change in breathing. One possibility is that the change in behavior is mediated via activation of locus coeruleus by breathing.[48] Nonetheless, we cannot rule out that the associated change in posture impacts the breathing rate based solely on pulmonary mechanics.

Our second claim is that movement and action relative to breathing, specifically the activation of neck and orofacial muscles, depends on behavioral state (Figures 5 and 7A). During foraging, the clavotrapezius, splenius, and biventer cervicis muscles are activated during inspiration, while the sternomastoid and cleidomastoid are recruited during expiration. These muscle synergies lead to an outward head rotation during expiration and an inward head rotation at the onset of inspiration. The switch from foraging to rearing is marked by an inversion of this organization, in which the phase shift with respect to breathing is nearly π radians while the phase difference between muscle groups is maintained (Figures 5B and 7A). The one exception is the clavotrapezius (Figure 5B). From the perspective of modulating sensation by motor output, it may be most reliable to issue commands to modulate separate pools of motoneurons that control head movement by binding them to a common rhythm.

Figure 4. Coordination of orofacial muscles with breathing during full arena search

(A) Illustration of the anatomy of vibrissa intrinsic (VI), nasolabialis (NL), and deflector nasi (DN) muscles. Asterisks indicate the approximate locations where the EMG is recorded.

(B) Example EMGs of bilateral intrinsic and deflector nasi muscles (gray), along with the processed data to yield the envelope of muscle activation, and the concurrent breathing and head yaw movements. Data from one rat.

(C) Example EMGs of bilateral nasolabialis muscles (gray); otherwise as above.

(D) Cross-correlation of the EMG envelopes of VI, NL, and DN muscles with respect to the onset of inspiration (sniffing, 4–14 Hz) and as a function of head pitch angle. Shaded areas indicate the standard errors. Data from individual rats. The timing of the whisking protractor (VI) is essentially unchanged as the rat changes state, while that for nose wiggling (DN) has the greatest change with state. Number of inspiration onsets (foraging/uncategorized/rearing): VI (5,146/1,391/801); NL (4,670/2,303/472); and DN (3,999/1,622/987).

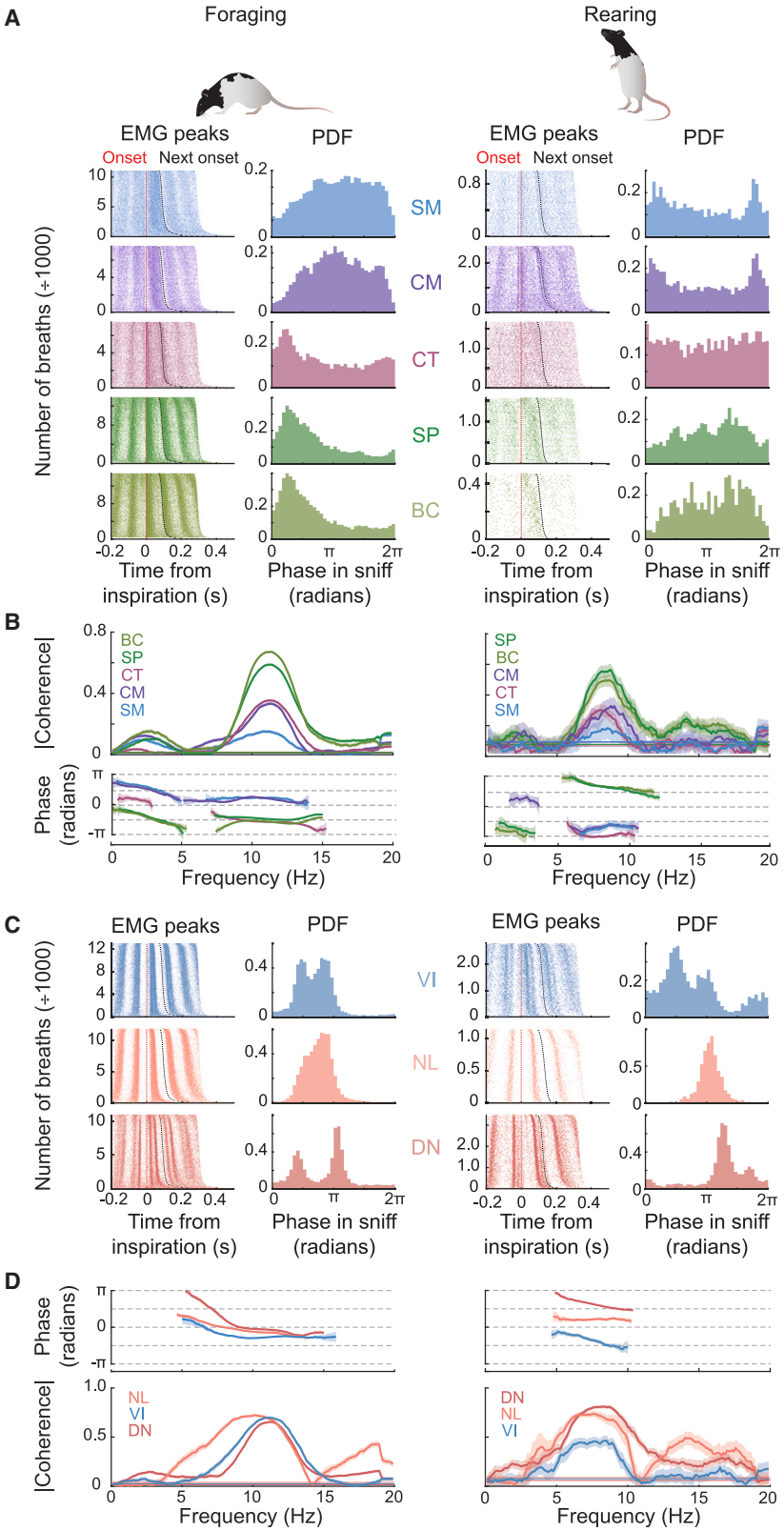

Figure 5. Quantification of the phase relation of neck and orofacial muscles to phase in the sniff cycle

(A) Raster plots of the neck EMG peaks with respect to the inspiration onsets (first and third columns), and the probability density functions (PDFs) of the neck EMG peaks in the sniffing cycles (second and fourth columns) during foraging (left 2 columns) and rearing (right 2 columns). Data shown from individual rats.

(B) Coherence of neck EMGs with breathing in the foraging (left) and rearing (right) states. Coherence calculated from segments of length 4 s, half-bandwidth of 1 Hz (7 tapers). Shaded areas are the standard errors found with a jackknife procedure. Horizontal lines indicate the 0.95 confidence levels. Foraging data: SM (1,803 segments from 7 rats), CM (2,039 segments from 8 rats), CT (3,013 segments from 11 rats), SP (2,557 segments from 10 rats), and BC (1,435 segments from 7 rats). Rearing data: SM (67 segments from 7 rats), CM (74 segments from 8 rats), CT (158 segments from 11 rats), SP (110 segments from 10 rats), and BC (115 segments from 7 rats).

(C) Raster plots of EMG peaks for vibrissa and nose movements with respect to the inspiration onsets, and the probability density function of EMG peaks in the sniffing (4–14 Hz) cycles. Data shown from individual rats.

(D) Coherence of vibrissa and nose EMGs with breathing; parameters as in (B). Data pooled from multiple rats (VI: 5, NL: 3, DN: 7). Shaded areas indicate the standard errors (jackknife). Horizontal lines show the 95% confidence levels. Number of segmented windows (foraging/rearing): VI (648/72), NL (288/55), and DN (1,668/122). See also Figure S2.

Please cite this article in press as: Liao and Kleinfeld, A change in behavioral state switches the pattern of motor output that underlies rhythmic head and orofacial movements, Current Biology (2023), https://doi.org/10.1016/j.cub.2023.04.008

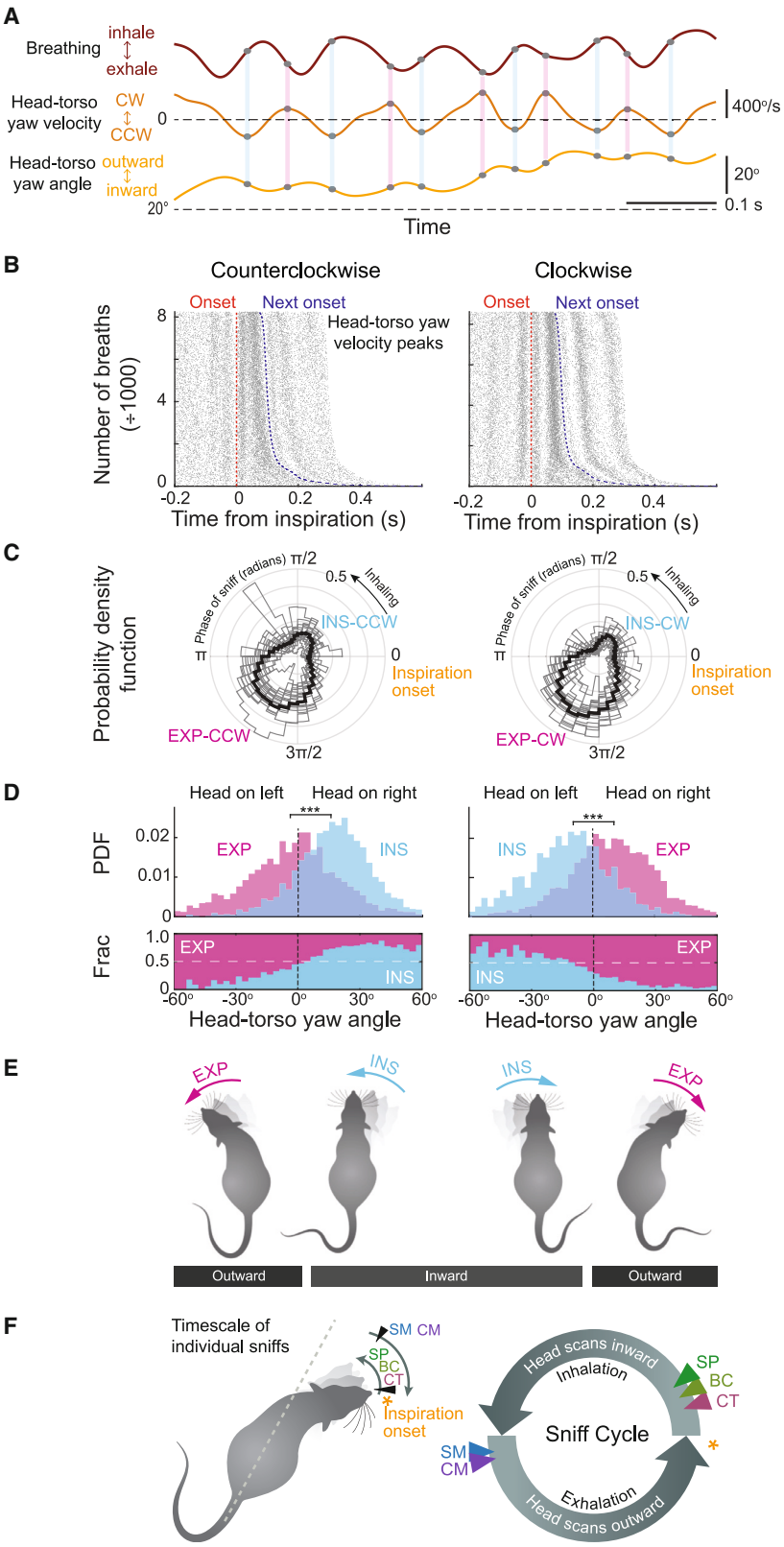

Figure 6. Inbound versus outbound horizontal head movements are preferentially biased to different phases in the breathing cycle

(A) Recording of breathing, head-torso yaw velocity, and head-torso yaw. Positive (clockwise) and negative (counterclockwise) peaks in the velocity data are marked.

(B) Raster plots of counterclockwise (CCW, left) and clockwise (CW, right) head-torso yaw velocity peaks with respect to the inspiration onsets. Rows are sorted by the periods of the breathing cycles. Red dashed line indicates the onsets of the breathing, and blue dashed line indicates the subsequent inspiration onsets. Data from one rat.

(C) Probability density function of the sniffing phase where the head-torso yaw velocity peaks (left: CCW, right: CW) occur, plotted in polar coordinates (17 rats). Black curve shows the results combined from all 17 rats. Windows of size $\pi/2$ radians centered at 0.96 and 4.28 radians define the regions of inspiratory (INS) and expiratory (EXP) head movements.

(D) Probability density function (upper) of the instantaneous head-torso yaw angle associated with inspiratory and expiratory head-wiggles (left, CCW; right, CW) and their fractional proportions (lower). Data from one rat. Head-torso yaw angle is defined to be positive (or negative) when the head is on the right (or left) of the torso midline. p value calculated using Kolmogorov–Smirnov test.

(E) Depiction of the postural dependency of the bimodal oscillations of the head. For both CW and CCW rotations, inward turns are more likely to occur with inspiratory breathing, while outward turns are more likely to occur with expiratory breathing.

(F) Depiction of head scanning with sequential activation of the neck muscles in the sniff cycle.

See also Figure S3.

Please cite this article in press as: Liao and Kleinfeld, A change in behavioral state switches the pattern of motor output that underlies rhythmic head and orofacial movements, Current Biology (2023), https://doi.org/10.1016/j.cub.2023.04.008

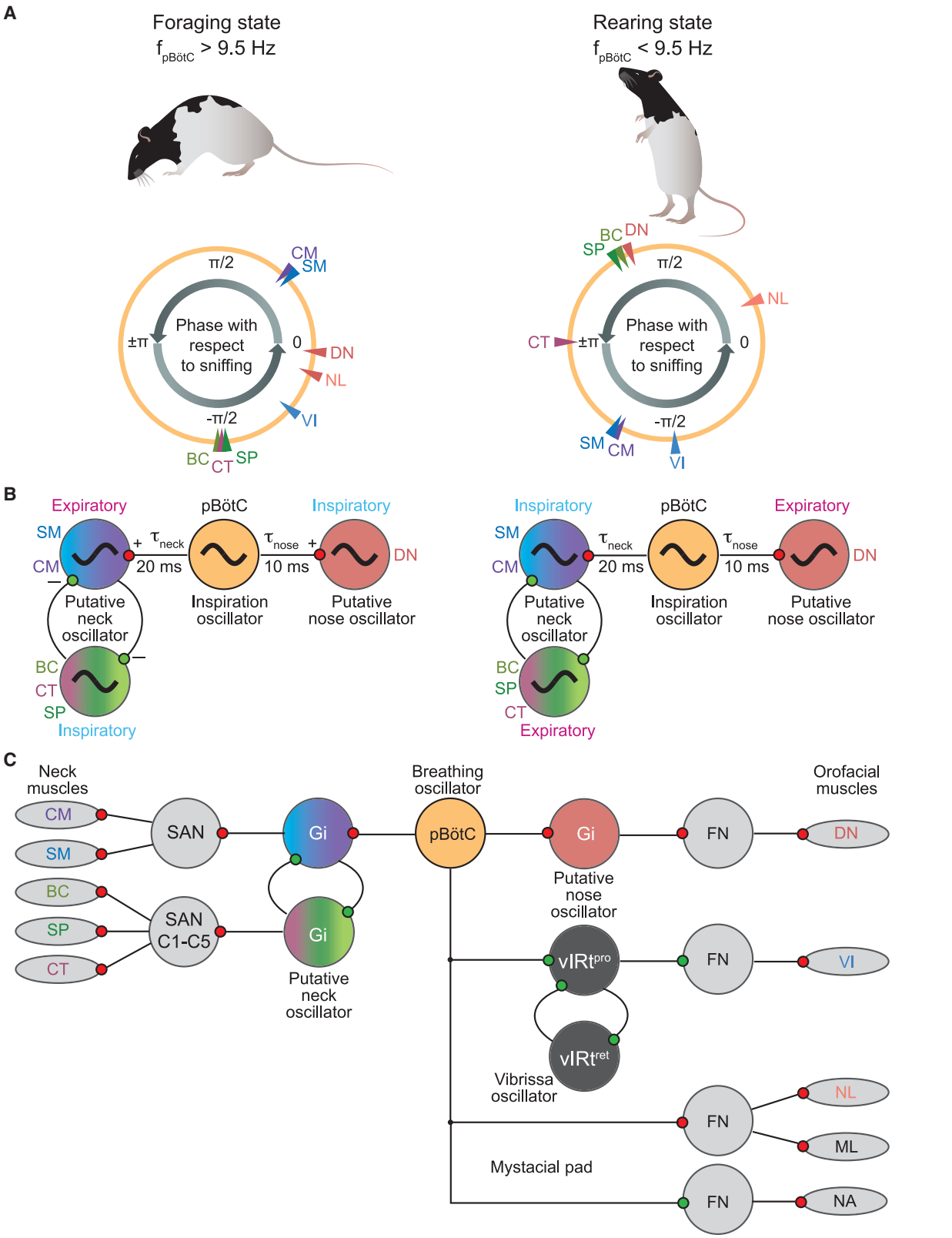

(legend on next page)

Please cite this article in press as: Liao and Kleinfeld, A change in behavioral state switches the pattern of motor output that underlies rhythmic head and orofacial movements, Current Biology (2023), https://doi.org/10.1016/j.cub.2023.04.008

All told, our results revealed a previously unrealized computational complexity that emerges from hindbrain circuits.

Our third claim is that the musculature involved in head turning and nose turning coordinate with breathing in a manner that respects the midline as an axis of symmetry (Figures 6E and 6F). The rat tends to turn outward for both CCW and CW rotations during expiration and turn inward toward the midline after the onset of inspiration. The observations that head yaw rotation during expiration has a greater average angular speed than rotation upon inspiration, and that the outward head rotation in egocentric coordinates occurs during expiration, are consistent with the notion that the expiratory phase of breathing is used to relocate the motor plant for a subsequent "snapshot" sample of the environment.[14,17,24] Recalling that the rat also uses the expiratory phase to relocate the head vertically,[14] the motor strategy of head movement is similar for both the vertical (pitch) and horizontal (yaw) axes.

Our work highlights the necessity for discovery based on the use of freely moving animals. In the current paradigm, the sniffing rate lies between 8 and 14 Hz (Figure 1H), as compared with a substantially lower rate of 4–8 Hz in studies with head-fixed rats.[14,17] The use of a large arena allowed the animal to readily change pose, with accompanying changes in breathing rate. A similar change in the rate of sniffing with a change in task occurs with rodents that sample an odor and then change state to respond with a head-poke and potentially receive a reward.[30] More complicated behavioral paradigms may lead to rodents taking on additional poses and reveal further complexity in the relation of motor actions to breathing.

Phase shift among behavioral states

Two changes occur as the rat alters its behavioral state from foraging to rearing. First, the central breathing frequency shifts from 11 to 8 Hz (Figure 1H). Second, the sternomastoid and cleidomastoid muscles shift their phase relationship with sniffing from expiratory to inspiratory activity, while the splenius and biventer cervicis muscles shift their phase relationship with sniffing from inspiratory to expiratory activity (Figures 3A and 5B). This combination of changes may be modeled by coupled phase oscillators[51] in which the spinal segments are taken as oscillators[12,52] and the interactions include time lags.[51,53]

Our model for coupling of neck movement to breathing has three oscillators (Figure 7B). The oscillator for inhalation, the pre-Bötzinger complex (pBötC),[54,55] has a variable output frequency that is taken as either $f_{pBötC} = f_{forage} = 11$ Hz for the foraging state or $f_{pBötC} = f_{rear} = 8$ Hz for the rearing state (Figure 1H). Two oscillators, connected with reciprocal, instantaneous inhibitory connections, represent the neck oscillators. Each neck oscillator drives one of the two antiphase subpopulations of neck motoneurons. The neck oscillators have an intrinsic frequency that is the mean value of $f_{pBötC}$, or $f_{neck} = (f_{forage} + f_{rear})/2 = 9.5$ Hz. A unilateral connection from the pBötC to one of the two neck oscillators has strength Γ_B and a time lag of τ_{neck}. We show (STAR Methods) that there are pairs of values for Γ_B and τ_{neck} for which the neck oscillator will shift in phase by π radians relative to the breathing oscillator when the frequency of sniffing changes between foraging and rearing. A delay of $\tau_{neck} = 20$ ms is mathematically feasible and is biologically plausible in terms of slow adaptation currents (Figure S4A). Further, the -0.75π radians phase offset between the two subgroups of neck oscillators is incorporated through the choice of the inhibitory connection strength.

The deflector nasi also shows a shift in coordination that depends on foraging versus rearing (Figure 5D). Premotor neurons of the deflector nasi have been identified in the reticular formation, and some receive the projections from the pBötC.[38] Thus, a similar analysis, except for only two oscillators, show that a frequency-dependent phase-locking holds for sniffing and nose wiggling (Figure 7B). Here, the pair with a shift in phase of 0.65π radians can be achieved with $\tau_{nose} = 10$ ms (Figure S4B).

All told, our analysis shows how, in principle, driving the sniffing rate at different frequencies will allow the rat to entrain the neck muscles at different phases in the sniff cycle to fulfill a specific behavioral need. There is no need for plastic changes in connectivity in the brainstem circuitry. The phase shifts can presumably be fine-tuned by neurobiological realism.[56]

Our model (Figure 7B) for understanding changes in the phase of orofacial motor actions relative to breathing is reminiscent of the coordinated shift in gait with increasing locomotion speed, and thus locomotor oscillator frequency, in tetrapods.[6,8,9,11] With regard to horses, the timing of opposing front and rear legs of the animal move in antiphase as the animal walks and trots, except that all four legs leave the surface during troting. In contrast, the opposing front and rear legs move in phase when a horse gallops. These dynamics, like those for head turning, can be modeled by coupled phase oscillators with fixed connectivity.[9]

Potential underlying neuronal circuit

The hierarchical arrangement that governs the impact of breathing on whisking was delineated over the past decade.[17,19,20,22] Two populations of inhibitory neurons in the vibrissa intermediate reticular formation form a network oscillator that can free run or be paced by projections from the pBötC.[54] Neighboring regions in the intermediate reticular formation likely contain putative oscillator circuits for the orofacial circuits that drive the

Figure 7. Summary of phase shifts and models

(A) Depiction of the phase relationship of neck and orofacial muscles with respect to breathing. Phase is defined from the coherence at the sniffing frequency (Figures 5B and 5D). Note the large changes for neck muscles (SM, sternomastoid; CM, cleidomastoid; CT, clavotrapezius; SP, splenius; BC, biventer cervicis), more modest change for the nose muscle (DN, deflector nasi), and small changes for the whisking (VI) and mystacial muscles (NL) during foraging versus rearing.

(B) Illustration of the interaction between breathing and head and nose movements using unidirectional coupling oscillators models. Red indicates excitatory synapses and green indicates inhibitory synapses in our model (STAR Methods).

(C) Cartoon of the known circuit for the control of rhythmic whisking[22] and potential circuit for the medullary control of head turning and nose movements.[49,50] New abbreviations: SAN, spinal accessory nucleus; C1–C5, spinal motonuclei at cervical levels from 1 to 5; Gi, Gigantocellular nucleus in the medulla; FN, facial motonucleus; $vIRt^{pro}$ and $vIRt^{ret}$, protraction and retraction subregions of the vibrissa premotor oscillator; ML and NA, maxillolabialis and nasalis muscles of the mystacial pad.

Please cite this article in press as: Liao and Kleinfeld, A change in behavioral state switches the pattern of motor output that underlies rhythmic head and orofacial movements, Current Biology (2023), https://doi.org/10.1016/j.cub.2023.04.008

muscles involved in licking,[57–61] chewing,[60,62–64] and nose twitching.[38]

The distributions of the motoneuron pools of the five neck muscles we examined (Figure 3A) have been well studied,[36,37] yet their premotor nuclei have not been fully investigated. It has been reported that there are no apparent direct projections from the pBötC to the spinal cord.[65] Therefore, the pathway of the respiratory drive for the neck muscles should involve premotor circuitry on the medulla, although relays of the respiratory oscillators[65,66] or the high cervical respiratory group in the cervical spinal cord[67,68] cannot be discounted.

Retrograde tracing with cholera toxin subunit B from sternomastoid revealed labeled neurons in the reticular formation.[69] Subsequent viral tracing studies localized the gigantocellular region of the reticular formation as a prospective location of neck premotor neurons, most likely V2a neurons.[49,50] These cells receive descending input from the contralateral superior colliculus, a high-level region that drives orienting and thus head position in rats.[70,71] In addition to the reticular formation, coordination between neck motoneurons may involve spinal interneurons in the propriospinal networks,[72] especially as microstimulation from vertebral levels C2 to T1 elicits sternomastoid activity.[73] In addition to connections from the pBötC to the gigantocellular premotor neurons for movement of the neck, there is some evidence for a similar pathway for rhythmic movement of the nose.[49] These potential connections, along with known, related connections for rhythmic movement of the vibrissa and the mystacial pad,[17,19,20] are summarized in Figure 7C.

Potential feedback control

Past studies identified the participation of sensory feedback in the control of whisking. The anatomical pathway involves vibrissa input to the spinal trigeminal subnuclei rostral interpolaris and oralis[74,75] that, in turn, project to vibrissa and mystacial motoneurons in the facial motor nucleus to complete a vibrissa-trigemino-facial reflex.[74–76] It is noteworthy that the prolonged, flat-top response as the rat's vibrissae contact the floor of the arena during foraging (* in Figure 4D), reminiscent of touch-induced "pump"[77,78] may be explained by a transient inhibitory reflex.[74] Lastly, neurons in spinal trigeminal oralis send projections to the cervical spinal cord.[79] This might serve as the substrate for coordinated movements of the vibrissae and the head to ensure proper timing of contact of the vibrissae to the ground in the sniff cycle.[46,80–82]

STAR★METHODS

Detailed methods are provided in the online version of this paper and include the following:

SUPPLEMENTAL INFORMATION

Supplemental information can be found online at https://doi.org/10.1016/j.cub.2023.04.008.

ACKNOWLEDGMENTS

We thank Rodolfo Figueroa for assistance with the instrumentation; Zaneta Ku, Peyton O'Callaghan, Emma Osgood, Sabrina Tuell, and Nina Zhang for animal training; Julia Kuhl for drawing all illustrations; Martyn Goulding, Jill Leutgeb, Fan Wang, Jing Wang, and Arash Fassihi Zakeri for conversations; and Beth Friedman and Philipp Mächler for comments on a draft manuscript. This work was supported by the Taiwan Ministry of Education Scholarship (GSSA) and the United States National Institutes of Health (R01 NS058668; U01 NS090595; U19 NS107466).

AUTHOR CONTRIBUTIONS

D.K. and S.-M.L. conceived the project and codeveloped the experimental approach, the instrumentation, the data analysis procedures, and the model. S.-M.L. performed all experiments and discovered the previously undescribed phase shifts with behavioral state. D.K. and S.-M.L. co-wrote the manuscript. D.K. attended to the myriad of university compliance rules and workshops that govern the ethical use of animals, environmental health and safety, research integrity and ethics, and the maintenance of a harassment-free work environment for all laboratory personnel.

DECLARATION OF INTERESTS

The authors declare no competing interests.

Received: January 12, 2023
Revised: March 27, 2023
Accepted: April 6, 2023
Published: April 26, 2023

REFERENCES

1. Ruder, L., and Arber, S. (2019). Brainstem circuits controlling action diversification. Annu. Rev. Neurosci. *42*, 485–504.
2. Moore, J.D., Kleinfeld, D., and Wang, F. (2014). How the brainstem controls orofacial behaviors comprised of rhythmic actions. Trends Neurosci. *37*, 370–380.
3. Arber, S., and Costa, R.M. (2022). Networking brainstem and basal ganglia circuits for movement. Nat. Rev. Neurosci. *23*, 342–360.
4. Grillner, S., Kozlov, A., Dario, P., Stefanini, C., Menciassi, A., Lansner, A., and Hellgren Kotaleski, J. (2007). Modeling a vertebrate motor system: pattern generation, steering and control of body orientation. Prog. Brain Res. *165*, 221–234.
5. Muybridge, E. (1957 (1899)) Animals in Motion (Dover).
6. Maes, L., and Abourachid, A. (2013). Gait transitions and modular organization of mammal locomotion. J. Exp. Biol. *216*, 2257–2265.
7. Dutta, S., Parihar, A., Khanna, A., Gomez, J., Chakraborty, W., Jerry, M., Grisafe, B., Raychowdhury, A., and Datta, S. (2019). Programmable coupled oscillators for synchronized locomotion. Nat. Commun. *10*, 3299.

8. Danner, S.M., Shevtsova, N.A., Frigon, A., and Rybak, I.A. (2017). Computational modeling of spinal circuits controlling limb coordination and gaits in quadrupeds. eLife *6*, e31050.
9. Collins, J.J., and Stewart, I.N. (1993). Coupled nonlinear oscillators and the symmetries of animal gaits. J. Nonlinear Sci. *3*, 349–392.
10. Buchli, J., and Ijspeert, A.J. (2008). Self-organized adaptive legged locomotion in a compliant quadruped robot. Auton. Robots *25*, 331–347.
11. Golubitsky, M., Stewart, I., Buono, P.L., and Collins, J.J. (1999). Symmetry in locomotor central pattern generators and animal gaits. Nature *401*, 693–695.
12. Kopell, N., and Ermentrout, G.B. (1988). Coupled oscillators and the design of central pattern generators. Math. Biosci. *90*, 87–109.
13. Welker, W.I. (1964). Analysis of sniffing of the albino rat 1). Behaviour *22*, 223–244.
14. Kurnikova, A., Moore, J.D., Liao, S.M., Deschênes, M., and Kleinfeld, D. (2017). Coordination of orofacial motor actions into exploratory behavior by rat. Curr. Biol. *27*, 688–696.
15. Karalis, N., and Sirota, A. (2022). Breathing coordinates cortico-hippocampal dynamics in mice during offline states. Nat. Commun. *13*, 467.
16. Kleinfeld, D., Deschênes, M., Wang, F., and Moore, J.D. (2014). More than a rhythm of life: breathing as a binder of orofacial sensation. Nat. Neurocience *17*, 647–651.
17. Moore, J.D., Deschênes, M., Furuta, T., Huber, D., Smear, M.C., Demers, M., and Kleinfeld, D. (2013). Hierarchy of orofacial rhythms revealed through whisking and breathing. Nature *497*, 205–210.
18. Moore, J.D., Deschênes, M., Kurnikova, A., and Kleinfeld, D. (2014). Activation and measurement of free whisking in the lightly anesthetized rodent. Nat. Protoc. *9*, 1792–1802.
19. Deschênes, M., Takatoh, J., Kurnikova, A., Moore, J.D., Demers, M., Elbaz, M., Furuta, T., Wang, F., and Kleinfeld, D. (2016). Inhibition, not excitation, drives rhythmic whisking. Neuron *90*, 374–387.
20. Takatoh, J., Prevosto, V., Thompson, P.M., Lu, J., Chung, L., Harrahill, A., Li, S., Zhao, S., He, Z., Golomb, D., et al. (2022). The whisking oscillator circuit. Nature *609*, 560–568.
21. Ranade, S., Hangya, B., and Kepecs, A. (2013). Multiple modes of phase locking between sniffing and whisking during active exploration. J. Neurosci. *33*, 8250–8256.
22. Golomb, D., Moore, J.D., Fassihi, A., Takatoh, J., Prevosto, V., Wang, F., and Kleinfeld, D. (2022). Theory of hierarchically organized neuronal oscillator dynamics that mediate rodent rhythmic whisking. Neuron *110*. 3833.e22–3851.e22.
23. Heck, D.H., McAfee, S.S., Liu, Y., Babajani-Feremi, A., Rezaie, R., Freeman, W.J., Wheless, J.W., Papanicolaou, A.C., Ruszinkó, M., Sokolov, Y., and Kozma, R. (2017). Breathing as a fundamental rhythm of brain function. Front. Neural Circuits *10*, 115.
24. Uchida, N., and Mainen, Z.F. (2003). Speed and accuracy of olfactory discrimination in the rat. Nat. Neurosci. *6*, 1224–1229.
25. Kluger, D.S., Balestrieri, E., Busch, N.A., and Gross, J. (2021). Respiration aligns perception with neural excitability. eLife *10*, e7090.
26. Allen, M., Varga, S., and Heck, D.H. (2022). Respiratory rhythms of the predictive mind.. Published online August 18, 2022. Psychol. Rev..
27. Tort, A.B.L., Brankačk, J., and Draguhn, A. (2018). Respiration-entrained brain rhythms are global but often overlooked. Trends Neurosci. *41*, 186–197.
28. Welzl, H., and Bures, J. (1977). Lick-synchronized breathing in rats. Physiol. Behav. *18*, 751–753.
29. Cao, Y., Roy, S., Sachdev, R.N., and Heck, D.H. (2012). Dynamic correlation between whisking and breathing rhythms in mice. J. Neurosci. *32*, 1653–1659.
30. Kepecs, A., Uchida, N., and Mainen, Z.F. (2007). Rapid and precise control of sniffing during olfactory discrimination in rats. J. Neurophysiol. *98*, 205–213.
31. Shik, M.L., Severin, F.V., and Orlovskiĭ, G.N. (1966). Control of walking and running by means of electric stimulation of the midbrain. Biofizika *11*, 659–666.
32. Leiras, R., Cregg, J.M., and Kiehn, O. (2022). Brainstem circuits for locomotion. Annu. Rev. Neurosci. *45*, 63–85.
33. Findley, T.M., Wyrick, D.G., Cramer, J.L., Brown, M.A., Holcomb, B., Attey, R., Yeh, D., Monasevitch, E., Nouboussi, N., Cullen, I., et al. (2021). Sniff-synchronized, gradient-guided olfactory search by freely moving mice. eLife *10*, e58523.
34. Wilson, J.J., Alexandre, N., Trentin, C., and Tripodi, M. (2018). Three-dimensional representation of motor space in the mouse superior colliculus. Curr. Biol. *28*. 1744.e12–1755.e12.
35. Bekele, A. (1983). The comparative functional morphology of some head muscles of the rodents Tachyoryctes splendens and Rattus rattus. II. Cervical Muscles Mamm. *47*, 549–572.
36. Brichta, A.M., Callister, R.J., and Peterson, E.H. (1987). Quantitative analysis of cervical musculature in rats: histochemical composition and motor pool organization. I. Muscles of the spinal accessory complex. J. Comp. Neurol. *255*, 351–368.
37. Callister, R.J., Brichta, A.M., and Peterson, E.H. (1987). Quantitative analysis of cervical musculature in rats: histochemical composition and motor pool organization. II. Deep dorsal muscles. J. Comp. Neurol. *255*, 369–385.
38. Kurnikova, A., Deschênes, M., and Kleinfeld, D. (2019). Functional brain stem circuits for control of nose motion. J. Neurophysiol. *121*, 205–217.
39. Hill, D.N., Bermejo, R., Zeigler, H.P., and Kleinfeld, D. (2008). Biomechanics of the vibrissa motor plant in rat: rhythmic whisking consists of triphasic neuromuscular activity. J. Neurosci. *28*, 3438–3455.
40. Haidarliu, S., Kleinfeld, D., Deschênes, M., and Ahissar, E. (2015). The musculature that drives active touch by vibrissae and nose in mice. Anat. Rec. (Hoboken) *298*, 1347–1358.
41. Dörfl, J. (1982). The musculature of the mystacial vibrissae of the white mouse. J. Anat. *135*, 147–154.
42. Dörfl, J. (1985). The innervation of the mystacial region of the white mouse. A topographical study. J. Anat. *142*, 173–184.
43. Deschênes, M., Haidarliu, S., Demers, M., Moore, J.D., Kleinfeld, D., and Ahissar, E. (2015). Muscles involved in naris dilation and nose motion in rat. Anat. Rec. (Hoboken) *298*, 546–553.
44. Hill, D.N., Curtis, J.C., Moore, J.D., and Kleinfeld, D. (2011). Primary motor cortex reports efferent control of vibrissa position on multiple time scales. Neuron *72*, 344–356.
45. Mitchinson, B., Martin, C.J., Grant, R.A., and Prescott, T.J. (2007). Feedback control in active sensing: rat exploratory whisking is modulated by environmental contact. Proc. Biol. Sci. *274*, 1035–1041.
46. Towal, R.B., and Hartmann, M.J. (2006). Right-left asymmetries in the whisking behavior of rats anticipate head movements. J. Neurosci. *26*, 8838–8846.
47. Latash, M.L. (2018). Muscle coactivation: definitions, mechanisms, and functions. J. Neurophysiol. *120*, 88–104.
48. Yackle, K., Schwarz, L.A., Kam, K., Sorokin, J.M., Huguenard, J.R., Feldman, J.L., Luo, L., and Krasnow, M.A. (2017). Breathing control center neurons that promote arousal in mice. Science *355*, 1411–1415.
49. Usseglio, G., Gatier, E., Heuzé, A., Hérent, C., and Bouvier, J. (2020). Control of orienting movements and locomotion by projection-defined subsets of brainstem V2a neurons. Curr. Biol. *30*. 4665.e6–4681.e6.
50. Cregg, J.M., Leiras, R., Montalant, A., Wanken, P., Wickersham, I.R., and Kiehn, O. (2020). Brainstem neurons that command mammalian locomotor asymmetries. Nat. Neurosci. *23*, 730–740.
51. Kuramoto, Y. (1984). Chemical Oscillations, Waves and Turbulence (Springer Verlag).
52. Holmes, P., Full, R.J., Koditschek, D., and Guckenheimer, J. (2006). The dynamics of legged locomotion: models, analyses, and challenges. SIAM Rev. *48*, 207–304.

53. Schuster, H.G., and Wagner, P. (1989). Mutual entrainment of two limit cycle oscillators with time delayed coupling. Prog. Theor. Phys. *81*, 939–945.

54. Smith, J.C., Ellenberger, H.H., Ballanyi, K., Richter, D.W., and Feldman, J.L. (1991). Pre-Bötzinger complex: a brainstem region that may generate respiratory rhythm in mammals. Science *254*, 726–729.

55. Feldman, J.L., Del Negro, C.A., and Gray, P.A. (2013). Understanding the rhythm of breathing: so near, yet so far. Annu. Rev. Physiol. *75*, 423–452.

56. Marder, E. (2012). Neuromodulation of neuronal circuits: back to the future. Neuron *76*, 1–11.

57. Travers, J.B., Dinardo, L.A., and Karimnamazi, H. (1997). Motor and premotor mechanisms of licking. Neurosci. Biobehav. Rev. *21*, 631–647.

58. Travers, J.B., DiNardo, L.A., and Karimnamazi, H. (2000). Medullary reticular formation activity during ingestion and rejection in the awake rat. Exp. Brain Res. *130*, 78–92.

59. Chen, Z., Travers, S.P., and Travers, J.B. (2001). Muscimol infusions in the brain stem reticular formation reversibly block ingestion in the awake rat. Am. J. Physiol. Regul. Integr. Comp. Physiol. *280*, R1085–R1094.

60. Stanek, E., 4th, Cheng, S., Takatoh, J., Han, B.X., and Wang, F. (2014). Monosynaptic premotor circuit tracing reveals neural substrates for oromotor coordination. eLife *3*, e02511.

61. Dempsey, B., Sungeelee, S., Bokiniec, P., Chettouh, Z., Diem, S., Autran, S., Harrell, E.R., Poulet, J.F.A., Birchmeier, C., Carey, H., et al. (2021). A medullary centre for lapping in mice. Nat. Commun. *12*, 6307.

62. Chandler, S.H., and Tal, M. (1986). The effects of brain stem transections on the neuronal networks responsible for rhythmical jaw muscle activity in the guinea pig. J. Neurosci. *6*, 1831–1842.

63. Nozaki, S., Iriki, A., and Nakamura, Y. (1986). Location of central rhythm generator involved in cortically induced rhythmical masticatory jaw-opening movement in the guinea pig. J. Neurophysiol. *55*, 806–825.

64. Nakamura, Y., and Katakura, N. (1995). Generation of masticatory rhythm in the brainstem. Neurosci. Res. *23*, 1–19.

65. Tan, W., Pagliardini, S., Yang, P., Janczewski, W.A., and Feldman, J.L. (2010). Projections of preBötzinger complex neurons in adult rats. J. Comp. Neurol. *518*, 1862–1878.

66. Dobbins, E.G., and Feldman, J.L. (1994). Brainstem network controlling descending drive to phrenic motoneurons in rat. J. Comp. Neurol. *347*, 64–86.

67. Oku, Y., Okabe, A., Hayakawa, T., and Okada, Y. (2008). Respiratory neuron group in the high cervical spinal cord discovered by optical imaging. NeuroReport *19*, 1739–1743.

68. Kobayashi, S., Fujito, Y., Matsuyama, K., and Aoki, M. (2010). Spontaneous respiratory rhythm generation in in vitro upper cervical slice preparations of neonatal mice. J. Physiol. Sci. *60*, 303–307.

69. Hayakawa, T., Takanaga, A., Tanaka, K., Maeda, S., and Seki, M. (2002). Ultrastructure and synaptic organization of the spinal accessory nucleus of the rat. Anat. Embryol. (Berl) *205*, 193–201.

70. Sahibzada, N., Dean, P., and Redgrave, P. (1986). Movements resembling orientation or avoidance elicited by electrical stimulation of the superior colliculus in rats. J. Neurosci. *6*, 723–733.

71. Dean, P., Redgrave, P., and Mitchell, I.J. (1988). Organisation of efferent projections from superior colliculus to brainstem in rat: evidence for functional output channels. Prog. Brain Res. *75*, 27–36.

72. Sunshine, M.D., Sutor, T.W., Fox, E.J., and Fuller, D.D. (2020). Targeted activation of spinal respiratory neural circuits. Exp. Neurol. *328*, 113256.

73. Sunshine, M.D., Ganji, C.N., Reier, P.J., Fuller, D.D., and Moritz, C.T. (2018). Intraspinal microstimulation for respiratory muscle activation. Exp. Neurol. *302*, 93–103.

74. Bellavance, M.A., Takatoh, J., Lu, J., Demers, M., Kleinfeld, D., Wang, F., and Deschênes, M. (2017). Parallel inhibitory and excitatory trigeminofacial feedback circuitry for reflexive vibrissa movement. Neuron *95*, 673–682.e4.

75. Nguyen, Q.T., and Kleinfeld, D. (2005). Positive feedback in a brainstem tactile sensorimotor loop. Neuron *45*, 447–457.

76. Pinganaud, G., Bernat, I., Buisseret, P., and Buisseret-Delmas, C. (1999). Trigeminal projections to hypoglossal and facial motor nuclei in the rat. J. Comp. Neurol. *415*, 91–104.

77. Deutsch, D., Pietr, M., Knutsen, P.M., Ahissar, E., and Schneidman, E. (2012). Fast feedback in active sensing: touch-induced changes to whisker-object interaction. PLoS One *7*, e44272.

78. Towal, R.B., and Hartmann, M.J. (2008). Variability in velocity profiles during free-air whisking behavior of unrestrained rats. J. Neurophysiol. *100*, 740–752.

79. Devoize, L., Doméjean, S., Melin, C., Raboisson, P., Artola, A., and Dallel, R. (2010). Organization of projections from the spinal trigeminal subnucleus oralis to the spinal cord in the rat: a neuroanatomical substrate for reciprocal orofacial-cervical interactions. Brain Res. *1343*, 75–82.

80. Grant, R.A., Sperber, A.L., and Prescott, T.J. (2012). The role of orienting in vibrissal touch sensing. Front. Behav. Neurosci. *9*, e00039.

81. Hobbs, J.A., Towal, R.B., and Hartmann, M.J.Z. (2015). Probability distributions of whisker–surface contact: quantifying elements of the rat vibrissotactile natural scene. J. Exp. Biol. *218*, 2551–2562.

82. Tsur, O., Khrapunsky, Y., and Azouz, R. (2019). Sensorimotor integration in the whisker somatosensory brain stem trigeminal loop. J. Neurophysiol. *122*, 2061–2075.

83. Prendergast, B.J., Onishi, K.G., and Zucker, I. (2014). Female mice liberated for inclusion in neuroscience and biomedical research. Neurosci. Biobehav. Rev. *40*, 1–5.

84. Levy, D.R., Hunter, N., Lin, S., Robinson, E.M., Gillis, W., Conlin, E.B., Anyoha, R., Shansky, R.M., and Datta, S.R. (2023). Mouse spontaneous behavior reflects individual variation rather than estrous state. Curr. Biol. *33*, 1–7.

85. Loeb, G.E., and Gans, C. (1986). Electromyography for Experimentalists (University of Chicago Press).

86. Mathis, A., Mamidanna, P., Cury, K.M., Abe, T., Murthy, V.N., Mathis, M.W., and Bethge, M. (2018). DeepLabCut: markerless pose estimation of user-defined body parts with deep learning. Nat. Neurosci. *21*, 1281–1289.

87. Nath, T., Mathis, A., Chen, A.C., Patel, A., Bethge, M., and Mathis, M.W. (2019). Using DeepLabCut for 3D markerless pose estimation across species and behaviors. Nat. Protoc. *14*, 2152–2176.

88. Insafutdinov, E., Pishchulin, L., Andres, B., Andriluka, M., and Schiele, B. (2016). DeeperCut: a deeper, stronger, and faster multi-person pose estimation model. In European Conference on Computer Vision, B. Leibe, J. Matas, N. Sebe, and M. Welling, eds. (Springer). https://doi.org/10.1007/978-3-319-46466-4_3.

89. He, K., Zhang, X., Ren, S., and Sun, J. (2016). Deep residual learning for image recognition. In 2016 IEEE Conference on Computer Vision and Pattern Recognition (CVPR), pp. 770–778.

90. Gal, O. (2022). fit_ellipse. https://www.mathworks.com/matlabcentral/fileexchange/3215-fit_ellipse.

91. Kleinfeld, D., and Mehta, S.B. (2006). Spectral mixing in nervous systems: experimental evidence and biologically plausible circuits. Prog. Theor. Phys. Suppl. *161*, 86–98.

92. Aljadeff, J., Lansdell, B.J., Fairhall, A.L., and Kleinfeld, D. (2016). Analysis of neuronal spike trains, deconstructed. Neuron *91*, 221–259.

93. Mitra, P.P., and Bokil, H.S. (2008). Observed Brain Dynamics (Oxford University Press).

Please cite this article in press as: Liao and Kleinfeld, A change in behavioral state switches the pattern of motor output that underlies rhythmic head and orofacial movements, Current Biology (2023), https://doi.org/10.1016/j.cub.2023.04.008

STAR★METHODS

KEY RESOURCES TABLE

REAGENT or RESOURCE	SOURCE	IDENTIFIER
Chemicals, peptides, and recombinant proteins		
Isoflurane	Henry Schein	Cat no. 1182097
Ketamine, Injection	Zoetis	Cat no. 40027676
Xylazine, Injection	AnaSed	Cat no. (01)00359399110204
Buprenorphine Hydrochloride, Injection	Par Pharmaceutical	Cat no. 110483373347
Experimental models: Organisms/strains		
Rat: Long-Evans	Charles River Laboratories	N/A
Software and algorithms		
MATLAB	MathWorks	N/A
Chronux	Cold Spring Harbor Laboratory	N/A
DeepLabCut	https://github.com/DeepLabCut/DeepLabCut	N/A
LabChart	AD Instruments	N/A
Pylon	Basler	N/A
Arduino IDE	Arduino	N/A
Teensyduino	https://www.pjrc.com/	N/A
BNO Library	Adafruit	N/A
Other		
Absolute Orientation Sensor	Adafruit	Cat no. BNO055
Microcontroller	https://www.pjrc.com/	Cat no. TEENSY3.2
CCD camera	Basler	Cat no. acA2040-90umNIR
PowerLab	AD Instruments	Cat no. 16/35
Differential amplifier (thermocouple)	World Precision Instruments	Cat no. DAM80
EMG Preamplifier	Kleinfeld Laboratory	https://neurophysics.ucsd.edu/lab/16_channel_ephys_second_stage.pdf
Current stimulator	A-M Systems	Cat no. 2100
Thermocouple	Omega	Cat no. 5TC-TT-K-36-36
Tungsten wire for electromyographs	A-M Systems	Cat no. 795500
10-pin connector	Samtec	Cat no. TMS-110-01-G-S-RA (M) Cat no. SMS-110-01-G-S (F) and SMS-110-01-L-S (F)

RESOURCE AVAILABILITY

Lead contact

Further information and requests for resources should be directed to and will be fulfilled by Prof. David Kleinfeld (dk@physics.ucsd.edu).

Materials availability

This study did not generate new unique reagents. The datasets supporting the current study are available from https://rhythm-n-rodents.github.io/.

Data and code availability

The datasets supporting the current study, and an associated "read me" file, are available from https://rhythm-n-rodents.github.io/.

Please cite this article in press as: Liao and Kleinfeld, A change in behavioral state switches the pattern of motor output that underlies rhythmic head and orofacial movements, Current Biology (2023), https://doi.org/10.1016/j.cub.2023.04.008

EXPERIMENTAL MODEL AND SUBJECT DETAILS

Experimental subjects

We used 33 Long Evans adult female rats ranging from 240 to 430 grams for this study. Variability across behavioral and physiological traits are not significantly greater in female rodents, including across the estrous cycle, than male rodents.[83,84] Behavioral training and surgical procedures were in accordance with the animal use protocol approved by the Institutional Animal Care and Use Committee (IACUC) at the University of California, San Diego.

Behavioral training

Animals (Long-Evans rats) were trained to forage for food under food restrictions. Before food restriction, body weight was measured to establish a baseline. Each food restriction period was no longer than five consecutive days. After five consecutive days of food restriction, animals had at least two days of ad libitum access to food.

Animals were weighed daily during the period of food restriction. Restriction ended immediately if the weight dropped below 0.8-times baseline. During the food restriction period, supplemental food was provided to ensure that the rats were not deprived of food for more than 24 h.

During the training and recording sessions, the rat was placed inside the foraging arena. Food pellets of $\sim$ 0.1 g were dropped into the arena one at a time at random locations after an auditory cue. The experiment ended when the rat no longer foraged for food.

Surgical procedures

All procedures were performed under anesthesia through the injection of ketamine (50 mg/kg-rat) and xylazine (5 mg/kg-rat). The level of anesthesia was monitored regularly by pinching the foot pad. Supplemental doses of ketamine (15 mg/kg-rat) and xylazine (1.5 mg/kg-rat) were provided when needed. An injection of buprenorphine (0.03-0.05 mg/kg-rat) was given before and after the surgery. At surgery, an incision was made along the midline above the skull to the nose. After cleaning the skull surface, 6 to 8 no. 00-90 screws (McMaster-Carr) were implanted. A hole (Bur Carbide FG ½, Henry Schein) was drilled on top of the nasal cavity, and a sterile thermocouple (5TC-TT-K-36-36, Omega) was inserted into the nasal cavity. The thermocouple wires were attached to the skull with Loctite 401 and Jet Acrylic (Lang Dental), and the end was soldered to a pair of 2.5 mm male pin connectors.

The electromyogram (EMG) electrodes were made with tungsten wires (#795500, A-M Systems). A pair of tungsten wires, with insulation removed at $\sim$1 mm at the tips, were aligned with a 1 to 3 mm distance between the bare tips, depending on the size of the target muscle. The tips of the electrodes were bent to create a hook. For EMG recordings in intrinsic vibrissae muscles, bipolar needle electrodes[85] were used, where the electrodes are passed through a 25-26G hypodermic needle. For EMG recordings in all other muscles, bipolar suture electrodes[85] were used, where the hook of the tungsten electrodes was tied to a silk suture. Electrodes were autoclaved before surgery. For implanting electrodes to the vibrissa intrinsic muscles, the hypodermic needle was passed subcutaneously from above the nasal bone to reach the vibrissae follicles. The needle was then gently retracted, leaving the electrodes in place. For implanting electrodes into all other muscles, surgical procedures were performed to expose the target muscle. Target muscles were identified using literature as references[35–37,39,43] and dissection studies (15 rats). The deflector nasi and nasolabialis muscles were accessed from above the nasal bone. Access from the dorsal neck was made to expose muscles splenius, biventer cervicis, and clavotrapezius. Access from the ventral neck was made to expose muscles sternomastoid and cleidomastoid. After exposing the target muscle, a silk suture was passed through the muscle belly gently to drag the electrodes into the muscle body. After exiting, the silk was tied back to the facia near the entry point to secure the location of the electrodes. We used electrical stimulation (Model 2100, A-M Systems) to confirm the location of the implanted electrodes by sending a pulse train of 0.2 ms duration, 4.8 ms burst width, and 1.2 ms inter-pulse period with 100 - 500 μA of current.[39] A reference electrode was made with a tungsten wire (#795500, A-M Systems), with $\sim$ 5 mm striped from the tip. The reference electrode was placed under the skin near the incision. The ground wire was made of a silver wire (#786000, A-M Systems) soldered to one of the head screws. Finally, the ends of the tungsten and silver electrodes were soldered to 10-pin male connectors (Samtec). All surgical incisions were closed with sutures.

In 17 animals, an orientation sensor was implanted into the torso subcutaneously between T1-T6 vertebrae by incision on the back. The torso sensor (BNO055, Adafruit) was covered with epoxy for insulation and sterilized. The surgical incision was closed with sutures. In all animals, a 10-pin female connector (Samtec) was fixed to the skull with Jet Acrylic. The head orientation sensor (BNO055, Adafruit) was attached to the connector before the start of each recording session. After surgery, animals were allowed to rest for at least two full days. Post-operative animals were checked regularly to monitor their conditions. Details of the procedures of each animal are listed in Table S1.

METHOD DETAILS

Video annotation and location tracking

As the rat was searching inside the arena, the entire process was recorded through a Basler camera (acA2040-90umNIR) above the arena at 20 fps. We used DeepLabCut,[86,87] a 2-D convolutional neural network-based algorithm, to track the animal's location. From each recording video, about 20 frames picked by DeepLabCut were manually labeled to mark the location of the rat's lower (sacral) torso. The labeled data were split into a 19:1 ratio for training and validation. We used a batch size of 1 and a learning rate of 0.005 with the SGD optimizer and trained a Resnet-50 model[88,89] for two iterations (20,000 epochs each). Other parameters were set to default.

Please cite this article in press as: Liao and Kleinfeld, A change in behavioral state switches the pattern of motor output that underlies rhythmic head and orofacial movements, Current Biology (2023), https://doi.org/10.1016/j.cub.2023.04.008

The tracking results were saved as a CSV file. To locate the center of the arena, we fitted the image of the floor boundary with an ellipse.[90]

We inspected all video files manually in order to label the frames where the rat performed miscellaneous behaviors, including scratching, dog-shaking, grooming, urinating, defecating, biting, and freezing. Data taken that these miscellaneous behaviors were not used in the analyses.

Data recording and pre-processing

The breathing signal was recorded from the rat by connecting the thermocouple to an amplifier (DAM80, World Precision Instruments). We used a 0.1 Hz high-pass filter, 100 Hz low-pass filter, and 10,000-times gain. The EMG signals were connected to a pre-amplification stage of local design to obtain a gain of ×400 and were high pass filtered at 0.1 Hz (https://neurophysics.ucsd.edu/lab/16_channel_ephys_second_stage.pdf). Breathing and EMG signals were sampled either at 20 kHz (27 rats) or 40 kHz (6 rats) with the data acquisition system (PowerLab, ADInstruments).

Head and torso orientation sensors (BNO055, Adafruit) were connected to a development board (Teensy 3.2, PJRC) via the I2C port. The orientation and movement signals from the head and torso sensors were read by Arduino code adopted from the Adafruit BNO055 library (https://github.com/adafruit/Adafruit_BNO055). Signals were sampled at 100 Hz, and the timestamps of each sample were sent to the breathing and EMG acquisition system with a pulse signal. Sensor data were displayed on the Arduino Serial Monitor and were saved to the hard drive at intervals no longer 7 min, and typically 6-½ min, at which time the head and torso sensors offsets drifted by less than one resolution unit or 0.01°. Ambiguities related to the wrapping of angular data across 0 to 2π radians led to the loss of 9.5 % of the data for egocentric yaw during foraging (Figure 6).

Pre-processing of data was done in MATLAB (MathWorks). First, we took the difference in the EMG signals between the pair of electrodes to obtain the differential EMG. The differential EMG was low pass filtered at 300 Hz by a third order Butterworth low-pass filter and high pass filtered at 9,999 Hz by a third order Butterworth high-pass filter. We then obtained the demodulated EMG envelope by taking the absolute value of the signal, low pass filtered at 50 Hz with a third-order Butterworth filter, and down-sampled to 2 kHz.

Digitized breathing data were low passed at 20 Hz with a fifth-order Butterworth filter, high passed at 1 Hz with a third-order Butterworth filter, and down-sampled to 2 kHz. The torso location-tracking data were low pass filtered at 4 Hz with a third-order Butterworth filter and were interpolated to 2 kHz with a cubic spline. The head and torso orientation data were interpolated to 20 kHz with a cubic spline. The head orientation data were low pass filtered at 25 Hz with a third-order Butterworth filter. The torso orientation data were low pass filtered at 4 Hz with a third-order Butterworth filter. All digital filters were run in both forward and reverse directions to obtain zero phase distortion. Finally, we took the difference between the head yaw and torso yaw to obtain the relative head-torso yaw, and we set the mean of the head-torso yaw angle of the entire recording to zero.

MODEL

Two-cell circuit

We analyze a dynamical system comprised of two phase-oscillators to model rhythmic nose twitching. We assume the connection between the two oscillators is unidirectional,[91] where only the nose oscillator is receiving signals from the breathing oscillator but not vice versa (Figure 7B). We consider a time lag constant τ and write

$$\frac{d}{dt}\Psi_B(t) = \omega_B \quad \text{(Equation 1)}$$

and

$$\frac{d}{dt}\Psi_N(t) = \omega_N + \Gamma_B \sin[\Psi_B(t-\tau) - \Psi_N(t)] \quad \text{(Equation 2)}$$

where $\Psi_B(t)$ is the phase of the breathing oscillator, in units of radians, and $\Psi_N(t)$ is the phase of the presumed nose oscillator. The coupling strength is denoted by Γ_B, the intrinsic frequency of the nose oscillator is denoted by ω_N, and the intrinsic frequency of the breathing oscillator is denoted by ω_B; all coupling strengths and frequencies are in units of rad/s. When two oscillators are phase-locked, we have

$$\omega_B - \omega_N = \Gamma_B \sin[\Psi_B(t-\tau) - \Psi_N(t)] \quad \text{(Equation 3)}$$

We make the ansatz that the solution takes the form of two oscillators that are locked at the breathing frequency, with a phase difference α. Thus

$$\Psi_B(t) = \omega_B t - \frac{\alpha}{2} \quad \text{(Equation 4)}$$

and

$$\Psi_N(t) = \omega_B t + \frac{\alpha}{2} \quad \text{(Equation 5)}$$

Please cite this article in press as: Liao and Kleinfeld, A change in behavioral state switches the pattern of motor output that underlies rhythmic head and orofacial movements, Current Biology (2023), https://doi.org/10.1016/j.cub.2023.04.008

Plugging Equations 4 and 5 into Equation 3 yields:

$$\alpha = \sin^{-1}\left(\frac{\omega_N - \omega_B}{\Gamma_B}\right) - \omega_B \tau. \quad \text{(Equation 6)}$$

The phase α corresponds to the phase between the breathing and nose oscillators and depends on two unknowns, Γ_B and τ. The solution exists, i.e., the breathing oscillator can entrain the nose oscillator, when

$$\Gamma_B \geq |\omega_N - \omega_B| \quad \text{(Equation 7)}$$

Stability analysis

The stability of the solutions in the model can be determined by adding a small perturbation to the steady-state solution of the nose oscillator, i.e.,

$$\Psi_N(t) = \Psi_N^{SS}(t) + \xi_N(t) \quad \text{(Equation 8)}$$

Substituting the right-hand-side of Equation 8, into Equations 2, 4 and 5 yields

$$\frac{d}{dt}\Psi_N(t) = \omega_N + \Gamma_B \sin[-\omega_B\tau - \alpha - \xi_N(t)]. \quad \text{(Equation 9)}$$

We expand the above equation for small magnitudes of $\xi_N(t)$ to:

$$\frac{d}{dt}\Psi_N(t) = \omega_N - \Gamma_B \sin(\omega_B\tau + \alpha) - \Gamma_B \cos(\omega_B\tau + \alpha)\xi_N(t) \quad \text{(Equation 10)}$$

Since

$$\frac{d}{dt}\Psi_N(t) = \frac{d}{dt}\Psi_N^{SS}(t) + \frac{d}{dt}\xi_N(t), \quad \text{(Equation 11)}$$

the steady state solution will factor out of Equation 10 and we obtain an equation for the perturbation, i.e.,

$$\frac{d}{dt}\xi_N(t) = -\Gamma_B \cos(\omega_B\tau + \alpha)\xi_N(t). \quad \text{(Equation 12)}$$

Substituting in Equation 6 yields

$$\frac{d}{dt}\xi_N(t) + \sqrt{\Gamma_B^2 - (\omega_N - \omega_B)^2}\,\xi_N(t) = 0 \quad \text{(Equation 13)}$$

and leads to a stable system, i.e., $\xi_N(t)$ decays to zero, by the existence criteria of Equation 7 for both foraging and rearing (Figure S4). Note that the recovery rate increases as the coupling strength increases.

Three-cell circuit

We analyze a dynamical system comprised of three phase oscillators to model rhythmic neck rotations. We assume a unilateral connection from the breathing oscillator to one of the two neck oscillators and reciprocal connections between the two neck oscillators (Figure 7B). We consider a time lag constant τ only for the unilateral connection and write

$$\frac{d}{dt}\Psi_B(t) = \omega_B, \quad \text{(Equation 14)}$$

$$\frac{d}{dt}\Psi_{N1}(t) = \omega_N + \Gamma_B \sin[\Psi_B(t-\tau) - \Psi_{N1}(t)] + \Gamma_N \sin[\Psi_{N2}(t) - \Psi_{N1}(t)], \quad \text{(Equation 15)}$$

and

$$\frac{d}{dt}\Psi_{N2}(t) = \omega_N + \Gamma_N \sin[\Psi_{N1}(t) - \Psi_{N2}(t)] \quad \text{(Equation 16)}$$

where the reciprocal coupling strength between neck muscles is denoted by Γ_N, and the intrinsic frequency of the neck oscillator is denoted by ω_N. When three oscillators are phase-locked, we have

$$\Gamma_N \sin[\Psi_{N2}(t) - \Psi_{N1}(t)] = -\frac{\Gamma_B}{2}\sin[\Psi_B(t-\tau) - \Psi_{N1}(t)] \quad \text{(Equation 17)}$$

and

$$\omega_B - \omega_N = \frac{\Gamma_B}{2}\sin[\Psi_B(t-\tau) - \Psi_{N1}(t)]. \quad \text{(Equation 18)}$$

Please cite this article in press as: Liao and Kleinfeld, A change in behavioral state switches the pattern of motor output that underlies rhythmic head and orofacial movements, Current Biology (2023), https://doi.org/10.1016/j.cub.2023.04.008

Similar to the case for two oscillators, we make the ansatz that the solution takes the form of three oscillators that are locked at the breathing frequency, with

$$\Psi_B(t) = \omega_B t - \frac{\alpha}{2} \quad \text{(Equation 19)}$$

$$\Psi_{N1}(t) = \omega_B t + \frac{\alpha}{2} \quad \text{(Equation 20)}$$

and

$$\Psi_{N2}(t) = \Psi_{N1}(t) + \beta \quad \text{(Equation 21)}$$

$$= \omega_B t + \frac{\alpha}{2} + \beta$$

Plugging Equations 19, 20, and 21 into Equations 17 and 18 yields:

$$\alpha = \sin^{-1}\left(2\,\frac{\omega_N - \omega_B}{\Gamma_B}\right) - \omega_B \tau \quad \text{(Equation 22)}$$

and

$$\beta = \sin^{-1}\left(\frac{\omega_N - \omega_B}{\Gamma_N}\right) \quad \text{(Equation 23)}$$

The phase α corresponds to the phase between the breathing and one population of neck oscillators and depends on two unknowns, Γ_B and τ. The phase β corresponds to the phase between the two populations of neck oscillators and depends on one unknown, Γ_N.

The solution exists when two criteria are satisfied. First, when:

$$|\Gamma_B| \geq 2|\omega_N - \omega_B| \quad \text{(Equation 24)}$$

and second, when

$$|\Gamma_N| \geq |\omega_N - \omega_B|. \quad \text{(Equation 25)}$$

Stability analysis

The analysis of the three-cell circuit divided into that of two pair-wise circuits. The stability of the breathing oscillator and nose oscillator pair was discussed previously. For the pair of neck oscillators, stability can be also determined by adding a small perturbation to the steady-state solution of the neck oscillators, i.e.,

$$\Psi_{N2}(t) = \Psi_{N2}^{SS}(t) + \xi_{N2}(t) \quad \text{(Equation 26)}$$

Substituting the right-hand-side of Equation 26, into Equation 16 yields

$$\frac{d}{dt}\Psi_{N2}(t) = \omega_N + \Gamma_N \sin\left[\Psi_{N1}^{SS}(t) - \Psi_{N2}^{SS}(t) - \xi_{N2}(t)\right]. \quad \text{(Equation 27)}$$

We expand the above equation for small magnitudes of $\xi_{N2}(t)$ and factor out the steady state response to obtain an equation for the perturbation, i.e.,

$$\frac{d}{dt}\xi_{N2}(t) + \Gamma_N \cos\left[\Psi_{N1}^{SS}(t) - \Psi_{N2}^{SS}(t)\right]\xi_{N2}(t) = 0 \quad \text{(Equation 28)}$$

or

$$\frac{d}{dt}\xi_{N2}(t) + \sqrt{\Gamma_N^2 - (\omega_N - \omega_B)^2}\,\xi_{N2}(t) = 0. \quad \text{(Equation 29)}$$

This leads to a stable system, i.e., $\xi_{N2}(t)$ decays to zero, when Equation 25 is satisfied. Further, phase shifts between $\Psi_{N1}(t)$ and $\Psi_{N2}(t)$ within the neighborhood of $\beta = \pi$ radians are achieved, by Equation 28, with $\Gamma_N < 0$. This implies mutual inhibition, for which $\pi/2 < \beta < 3\pi/2$, with $\beta \rightarrow \pi$ as $\Gamma_N \rightarrow -\infty$.

Please cite this article in press as: Liao and Kleinfeld, A change in behavioral state switches the pattern of motor output that underlies rhythmic head and orofacial movements, Current Biology (2023), https://doi.org/10.1016/j.cub.2023.04.008

Application

The shift in the phase between foraging and rearing corresponds to the shift in α between these two states. We assume that $\omega_B = 22\pi$ rad/s (11 Hz) during foraging and $\omega_B = 16\pi$ rad/s (8 Hz) during rearing (Figure 1H). We further assume that all coupling strengths and the intrinsic frequency of all but the breathing oscillator are constants.

Breathing drives the neck oscillator

Our measurements of the shift in phase correspond to the difference $\alpha^{forage} - \alpha^{rear}$. From Equation 22,

$$\alpha^{forage} - \alpha^{rear} = \sin^{-1}\left(2\frac{\omega_N - \omega_B^{forage}}{\Gamma_B}\right) - \sin^{-1}\left(2\frac{\omega_N - \omega_B^{rear}}{\Gamma_B}\right) - \left(\omega_B^{forage} - \omega_B^{rear}\right)\tau \quad \text{(Equation 30)}$$

which is one equation in two unknowns, i.e., τ and Γ_B. From the data, $\alpha^{forage} - \alpha^{rear} = \pi$ (Figure 5B) and we assume $\omega_N = 19\pi$ rad/s (9.5 Hz), chosen as the midpoint frequency between rearing and foraging (Figure 1H). We solve Equation 30 numerically to find all pairs of values of τ and Γ_B (Figure S4A). From Equation 24, the magnitude of Γ_B is bounded by $\Gamma_B \geq 6\pi$ rad/s. A plausible pair of solutions is $\tau = 20$ ms and $\Gamma_B = 19.2$ rad/s.

The phase shift among the two neck oscillators is observed to be $\beta = -0.75\pi$ (Figure 5B). We find $\Gamma_N = -13.2$ rad/s from Equation 23.

Breathing drives the nose oscillator

This analysis is similar to that for the neck except for a numerical difference in formula (Equation 6). Thus

$$\alpha^{forage} - \alpha^{rear} = \sin^{-1}\left(\frac{\omega_N - \omega_B^{forage}}{\Gamma_B}\right) - \sin^{-1}\left(\frac{\omega_N - \omega_B^{rear}}{\Gamma_B}\right) - \left(\omega_B^{forage} - \omega_B^{rear}\right)\tau \quad \text{(Equation 31)}$$

From the data, $\alpha^{forage} - \alpha^{rear} = 0.65\pi$ (Figure 5D) and as above we assume $\omega_N = 19\pi$ rad/s (9.5 Hz). We solve Equation 31 numerically to find all pairs of values of τ and Γ_B (Figure S4B). From Equation 7, the magnitude of Γ_B is bounded by $\Gamma_B \geq 3\pi$ rad/s. A plausible pair of solutions is $\tau = 10$ ms and $\Gamma_B = 11.8$ rad/s.

DATA ANALYSIS

We used MATLAB (MathWorks) code for data analysis.[92] Spectral analyses were performed with Chronux (http://chronux.org/).[93] To define the inspiration onsets, we followed the procedures from a previous studies: the Hilbert transform was applied on the thermocouple signal to extract all the local peaks (maximal inhalation) and troughs (maximal exhalation),[44] and the inspiration onsets were defined to be the 10 % rise times from each trough.[17] The peaks in the movement signals, recorded from head or torso orientation sensor, were identified by setting the 75th percentile value as the minimum height threshold and the 0.5 x std as the minimum prominence; percentiles and std were calculated from all recording sessions in the same rat. The peaks in the EMG envelopes were identified by setting the 90th percentile value as the minimum height threshold, the 99.99th percentile value as the maximum height threshold, and the 0.5 x std as the minimum prominence; percentiles and std were calculated from all recording sessions in the same rat.